Formation of Corrugated *n* = 1 2D Tin Iodide Perovskites and Their Use as Lead-Free Solar Absorbers

Benny Febriansyah,[a],[b],[c] Yulia Lekina,[d] Jagjit Kaur,[e] Thomas J. N. Hooper,[f] Padinhare Cholakkal Harikesh,[b],[c] Teddy Salim,[g] Ming Hui Lim,[a] Teck Ming Koh,[b] Sudip Chakraborty,[e]* Ze Xiang Shen,[b],[d]* Nripan Mathews,[b],[g]* Jason England[a]*

[a] Division of Chemistry and Biological Chemistry, School of Physical and Mathematical Sciences, Nanyang Technological University, 21 Nanyang Link, Singapore 637371, Singapore.

[b] Energy Research Institute at Nanyang Technological University (ERI@N), Research Techno Plaza, X-Frontier Block Level 5, 50 Nanyang Drive, Singapore 637553, Singapore.

[c] Interdiscipinary Graduate School (IGS), 50 Nanyang Avenue, Singapore 639798 Singapore

[d] Division of Physics and Applied Physics, School of Physical and Mathematical Sciences, Nanyang Technological University, 21 Nanyang Link, Singapore 637371, Singapore.

[e] Materials Theory for Energy Scavenging (MATES) Lab, Discipline of Physics, Indian Institute of Technology Indore, Simrol, Indore 453552, India.

[f] Centre of High Field Nuclear Magnetic Resonance (NMR) Spectroscopy and Imaging, Nanyang Technological University, 21 Nanyang Link, Singapore 637371, Singapore.

[g] School of Materials Science and Engineering, Nanyang Technological University, 50 Nanyang Avenue, Singapore 639798, Singapore.

ABSTRACT: Major strides have been made in the development of materials and devices based around low-dimensional hybrid group 14 metal halide perovskites. Thus far, this work has mostly focused upon compounds containing highly toxic Pb, with the analogous less toxic Sn materials being comparatively poorly evolved. In response, the study herein aims to (i) provide insight into the impact of templating cation upon the structure of *n* = 1 2D tin iodide perovskites (where *n* refers to the number of contiguous two-dimensional (2D) inorganic layers, *i.e.*, not separated by organic cations), and (ii) examine their potential as light absorbers for photovoltaic (PV) cells. It was discovered through systematic tuning of organic dications, that imidazolium rings are able to induce formation of (*110*)-oriented materials, including the examples of "3 × 3" corrugated Sn-I perovskites. This structural outcome is a consequence of a combination of supramolecular interactions of the two endocyclic N-atoms in the imidazolium functionalities with the Sn-I framework and the higher tendency of Sn^{2+} ions to stereochemically express their $5s^2$ lone pairs relative to the $6s^2$ electrons of Pb^{2+}. More importantly, the resulting materials feature very short separations between their 2D inorganic layers with iodide–iodide (I···I) contacts as small as 4.174 Å, which is amongst the shortest ever recorded for 2D tin iodide perovskites. The proximate inorganic distances, combined with the polarizable nature of the imidazolium moiety, eases the separation of photogenerated charge within the materials. This is evident from the excitonic activation energies as low as 83(10) meV, measured for ImEA[SnI_4]. When combined with superior light absorption capabilities relative to their lead congeners, this allowed fabrication of lead-free solar cells with incident photon-to-current and power conversion efficiencies of up to 70 % and 2.26 %, respectively, which are amongst the highest values reported for pure *n* = 1 2D group 14 metal halide perovskites. In fact, these values are superior to the corresponding lead iodide material, which demonstrates that 2D Sn-based materials have significant potential as less toxic alternatives to their Pb counterparts.

KEYWORDS: *2D perovskites, iodostannates, lead-free, solar cells, crystal engineering, lone pair steric activity*

Hybrid organic-inorganic lead halide perovskites have shown promise in a range of optoelectronic applications. Most prominently, the use of the three-dimensional (3D) material (A)PbX_3 (where A is a relatively small monocation, such as methylammonium (MA^+) and formamidinium (FA^+), and X is bromide or iodide) as a light absorbing layer has allowed development of photovoltaic cells displaying power conversion efficiencies (PCEs) of up

to 25.2 %.[1] This, combined with their solution processability, makes them highly attractive and has led to intensive study of their properties and applications. On the downside, major challenges are posed by the high toxicity of water-soluble Pb^{2+}, which can contaminate groundwater during processing or as a consequence of module damage.[2] This has spurred investigations into replacement of Pb with less toxic elements, such as Sn or Ge. While examples of hybrid perovskites containing each of these alternatives is known and recent reports have demonstrated that they can be stabilized,[3-6] Ge halide perovskites seem less promising due to the very poor inherent chemical stability of Ge^{2+}.[7-8] On the other hand, Sn-based perovskites are more desirable due to the similarity of their electronic and optical properties to Pb perovskites and their relatively eco-friendly degradation product, SnO_2.[9] Thus, concerted efforts have been made to enhance the efficiency and stability of tin halide-based 3D perovskites *via* a variety of approaches, including utilization of antioxidants,[10-11] reducing agents,[12-13] and mixed-cation compositions.[14-15] This has resulted in solar cell devices with certified PCEs of over 10 % that can maintain more than 90 % of their initial efficiency upon storage or after operation at the maximum power point for over 1000 hours.[4-6] However, while numerous research groups have contributed to development of 3D $(A)SnX_3$ perovskites for use in photovoltaic applications, the number of publications reporting the development and fundamental properties of Sn-based materials, particularly those of lower dimensionalities, remain relatively small.

Two-dimensional (2D) hybrid metal halide perovskites possessing the general chemical formulae $(RNH_3)_2BX_4$ and $(NH_3RNH_3)BX_4$ (R corresponds to an organic functional group, B a group 14 metal dication, and X a halide) are derived from their 3D congeners by slicing the inorganic lattice along specific crystallographic axes (*e.g.,* the (*100*)- or (*110*)-planes).[16-17] This can be induced through incorporation of moderately-sized organic cations, such as the omnipresent phenylethylammonium (PEA^+) and 1-butylammonium (BA^+) ions, and it yields alternating 2D layers of organic cations and single Pb-atom-thick inorganic lattices. These are referred to as $n = 1$ 2D hybrid metal halide perovskites, where n refers to the number of contiguous two-dimensional (2D) inorganic layers, *i.e.*, not separated by organic cations. The advantages of reduced dimensionality are multifold. First, the incorporation of inherently more hydrophobic organic cations grants improved intrinsic stability against degradation by moisture and oxygen.[18-19] In addition, the larger formation energy of the low-dimensional inorganic lattices,[20-21] combined with the relatively bulky organic species, renders the materials less prone to ionic migration and, thereby, reduces their electrical instability. Last but not least, it affords significant room for materials exploration and engineering. This is because the size constraints imposed on the organic cations by 3D perovskite formation (typically assessed by Goldschmidt's tolerance factor) are no longer relevant.[22-23]

Being initially considered ill-suited for PV applications due to electronic and quantum confinement,[24-25] molecular engineering of the organic cations that template $n = 1$ 2D inorganic lattice formation has led to tremendous advancements in the PCEs of solar cells based on this class of materials. Several exemplary works are worthy of mention. First is the demonstration by Stupp and co-workers[18] of enhanced out-of-plan conductivity in 2D perovskites through the incorporation of suitable conjugated organic spacers (*e.g.,* pyrene and perylene), which resulted in pure 2D perovskite solar cells with a PCE of 1.38%. The second one was reported by our group,[26] wherein we used compact pyridinium and imidazolium dications to template 2D lead iodide perovskites featuring reduced inter-octahedral distortion and inorganic interlayer separation. This allowed PCEs of up to 1.83% to be achieved. Through further fine-tuning of the inorganic lattice inter-octahedral geometry and layer separation using the 2-cyanoethan-1-aminium (3-APN) templating cation, and energy level alignment within the device, Wang and co-workers were very recently able to report a highly efficient pure $n = 1$ 2D perovskite solar cell possessing a PCE of 3.39 %.[19]

The aforementioned examples of PV devices incorporating $n = 1$ 2D perovskite solar absorbing materials are all Pb-based. Unfortunately, comprehensive studies dedicated to the synthesis and characterization of less toxic $n = 1$ 2D tin halide perovskites are comparatively rare. More crucially, as far we are aware, there has only been one report of a PV device using a $n = 1$ 2D halostannate as a solar absorber.[27] The material in question, $Bn_2[SnI_4]$ (Bn = benzimidazolium), afforded a device efficiency of around 2.3 %. This suggests that these materials have promise, but further examples are required to verify this and provide insight into the molecular design principles that control 2D tin halide lattice structure. As can be seen from their Pb-based counterparts, lattice structure controls photophysical properties of metal halide perovskites, so understanding how they can be tailored is of critical importance for the development of devices with high photovoltaic efficiency.

Most 2D halostannates reported thus far are of the (*100*)-oriented type, with more than 50 having been documented in the Cambridge Structural Database. Therein, the $[SnX_6]^{4-}$ octahedra corner-share their four equatorial vertices and the remaining two axial halides are terminally bound. This affords "flat" inorganic layers. On the other hand, corrugated (*110*)-oriented structures, which additionally contain $[SnX_6]^{4-}$ octahedra possessing two *cis*-oriented terminally-bound halides, are much rarer. In fact, we are aware of only 2 examples, both iodostannates, having been published thus far. The first, reported in 1999 by Guloy and co-workers,[28] incorporated the dication $[NH_3(CH_2)_5NH_3]^{2+}$ as a template; and the second, disclosed 17 years later by Kanatzidis and co-workers,[29] used doubly-protonated histamine (HA^{2+}). Both of these compounds, α-$NH_3(CH_2)_5NH_3[SnI_4]$ and α-$HA[SnI_4]$, feature "4 × 4" corrugated structures, where "n × n" refers to the number (n) of contiguous Sn octahedra comprising each ridge. Thus, systematic structural and photophysics investigations of (*110*)-oriented 2D tin halide perovskites are almost non-existent. By extension, we are uncertain about how the structure of organic cations influences formability of the lattice and

how this impacts the optoelectronic properties of these materials.

Spurred by these considerations, we utilized the ditopic organic dication 1-(2-ammonioethyl)-1*H*-imidazol-3-ium ($ImEA^{2+}$) to template the formation of the 2D tin iodide perovskite $ImEA[SnI_4]$. $ImEA^{2+}$ was selected because we have previously shown that it is able to selectively induce formation of rare corrugated lead halide structures.[26, 30] In addition, relatively efficient pure $n = 1$ 2D lead-based perovskite solar cells with good current generation were obtained using this dication.[26] As such, it not only serves as an excellent platform for investigation of the formability of (*110*)-oriented structural motifs, along with their accompanying optoelectronic properties, but also enables a direct comparison of the impact of Sn *versus* Pb upon the photovoltaic performance of 2D perovskites to be made.

RESULTS AND DISCUSSION

Imidazolium cores and their role in formation of corrugated structures. To synthesize the target compound, $ImEA(I)_2$ was combined with SnI_2 in hot hydroiodic acid under an inert atmosphere. Slow cooling of the solution led to formation of dark maroon colored crystals. X-ray crystallographic analysis of the compound formed, $ImEA[SnI_4]$, yielded the structure displayed in **Figure 1**. (Crystallographic and structure refinement data appear in **Tables S1-S3**.) As observed in the corresponding Pb-I compound, a "3 × 3" (*110*)-oriented 2D structure, composed of alternating inorganic and organic monolayers, was observed. The distances between its constituent inorganic layers are very short, which can be attributed to the compact nature of the dication and flexibility of the ammonioethyl pendant. Indeed, the shortest I···I interlayer contacts in this structure, of 4.174 Å, are amongst the shortest ever recorded for 2D tin iodide perovskites. For comparison, the flexible organic cations *N*¹,*N*¹,*N*¹-trimethylethane-1,2-diaminium,[31] 1,5-pentanediammonium,[32] and 1-butylammonium[30] impart closest I···I contacts of 4.186, 4.587, and 8.668 Å, respectively. Meanwhile, the more rigid cations biimidazolium,[33] benzodiimidazolium,[27] and benzimidazolium[34] yield respective I···I closest contacts of 4.444, 4.855, and 8.077 Å.

Each asymmetric unit of $ImEA[SnI_4]$ contains two inequivalent $ImEA^{2+}$ dications (**Figure S1**), which differ in terms of conformation and interactions with the iodostannate lattice. H-bonding interactions between the primary ammonium and imidazolium N-H groups and their neighboring iodide ions (N···I contacts ranging from 3.586 to 4.257 Å; **Figure 1b**) are observed in both conformations. In addition, the structure features coulombic interactions between the alkylated endocyclic N-atoms of the $ImEA^{2+}$ dications and terminally-bound iodides that are oriented perpendicular to the plane of the imidazolium ring (N···I contacts of 3.680 and 3.924 Å).

Interestingly, attempts to induce similar (*110*)-oriented 2D tin iodide structures using templating dications comprised of pyridinium substituted at various positions by 2-ethylammonium pendant groups were unsuccessful. In all

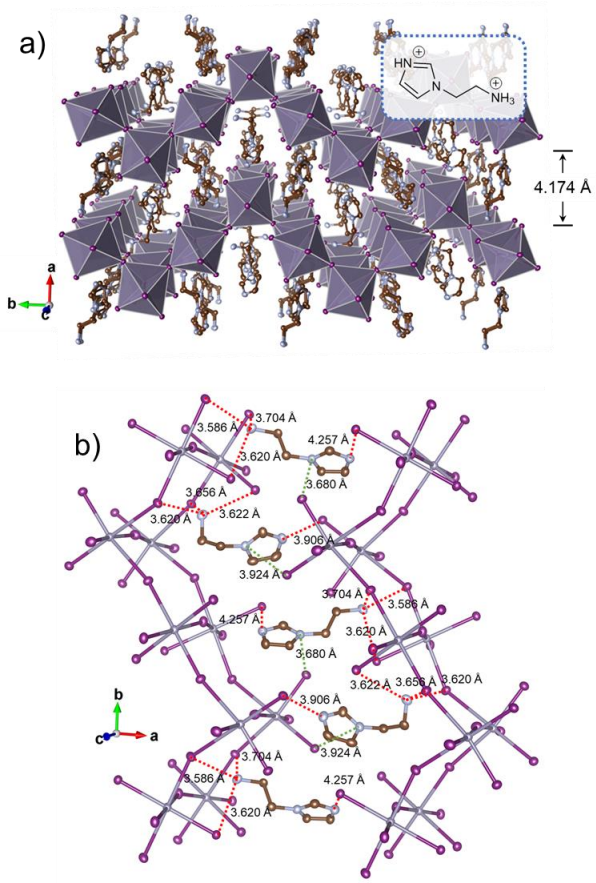

Figure 1. a) X-ray crystal structure of "3 × 3" (*110*)-oriented 2D perovskite $ImEA[SnI_4]$. The inset shows the molecular structure of $ImEA^{2+}$. b) X-ray crystal structure of $ImEA[SnI_4]$ highlighting the closest contacts between the primary ammonium and imidazolium NH^+ N-atoms of $ImEA^{2+}$ and the bridging/terminal I^- ions of the iodostannate lattice (dashed red lines). The closest contacts between the alkylated endocyclic N atoms of $ImEA^{2+}$ and terminally bound I^- ions are depicted using dashed green lines. Lavender, purple, brown, and blue spheroids represent Sn, I, C, and N atoms, respectively. H atoms are omitted for clarity. Ellipsoids are shown at 50% probability.

cases, (*100*)-type 2D structures are obtained (**Figures 2a-d**). Although the larger ring size of pyridinium may play a role in determining the inorganic architecture, we believe the deciding factor is the additional H-bonding interaction with the imidazolium ring, which is a consequence of having two endocyclic N-atoms. The extra intermolecular interactions that this provides are sufficient to stabilize the, seemingly, less stable corrugated structure. This notion is supported by the observation that isomeric imidazolium-based dication 2-(2-ammonioethyl)-1*H*-imidazol-3-ium (2-ImEA), also, templates formation of a "3 × 3" (*110*)-oriented 2D tin iodide perovskite (**Figure 2f**). Therein, the observed N···I contacts, ranging from 3.457 to 3.685 Å, are even shorter than those observed in $ImEA[SnI_4]$ (see **Figure S2** for more details).

We sought to corroborate this conclusion by examining the structure of the previously reported compound

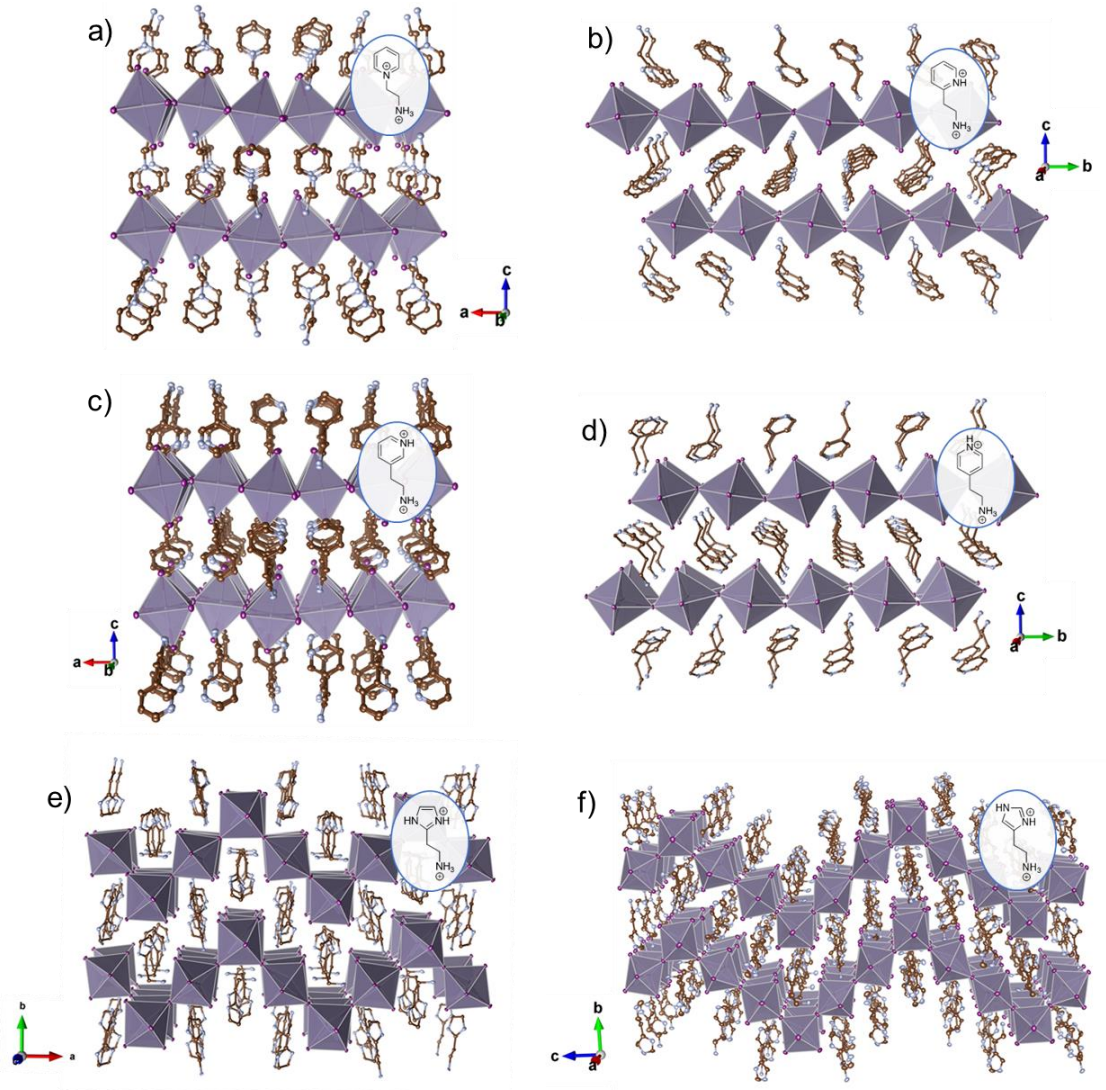

Figure 2. X-ray crystal structures of the pyridinium-based (*100*)-oriented 2D tin iodide perovskites a) PyrEA[SnI_4], b) 2-PyrEA[SnI_4], c) 3-PyrEA[SnI_4], and d) 4-PyrEA[SnI_4] and their imidazolium-based (*110*)-oriented congeners, e) 2-ImEA[SnI_4], and f) HA[SnI_4]. Lavender, purple, light brown and light blue spheroids correspond to Sn, I, C and N atoms, respectively. H atoms are omitted for clarity. Thermal ellipsoids are shown at 50% probability. The insets show the aryl component of the templating dications.

HA[SnI_4] (see **Figure 2g**).[29] However, it has not been deposited into the Cambridge Structural Database. In response, we proceeded to synthesize this material and solve its single crystal X-ray structure. Under our synthetic conditions, it exists exclusively in a "4 × 4" (*110*)-type orientation and is stable for months both in the mother liquor and dry, as long as the inert atmosphere is provided. This is surprising given that conversion to a thermodynamically stable (*100*)-oriented phase was reported to occur upon leaving HA[SnI_4] in the crystallization mother liquor.[28] Regardless, all of the ethylammonium-substituted imidazolium dications are found to template corrugated iodostannate motifs, while their pyridinium counterparts yield flat lattices.

Stereochemical activity of Sn(II) and Pb(II) s orbital electrons. The preceding structural trends do not hold true for the corresponding iodo- and bromoplumbates. Instead, corrugated n = 1 2D perovskites were obtained only for $ImEA^{2+}$ (**Figures S3 and S4**), with the hybrids templated by 2-$ImEA^{2+}$ and HA^{2+} adopting (*100*)-type orientations.[26, 30, 35-36] Thus, in addition to the supramolecular interactions between their constituent organic and inorganic components, it appears that the composition of the metal halide framework is also a determining factor in whether (*110*)-oriented structures form. Comparison of trends in the metal halide bond lengths and displacement of the metal ions from the centre of their pseudo-octahedral coordination spheres for a series of similarly templated Pb and Sn halides shed light on the origin of these observations.

It is clear from **Figure 3** (see **Tables S4-S24** for the complete list of data) that the distribution of metal halide bond distances in the iodostannate and bromoplumbate lattices

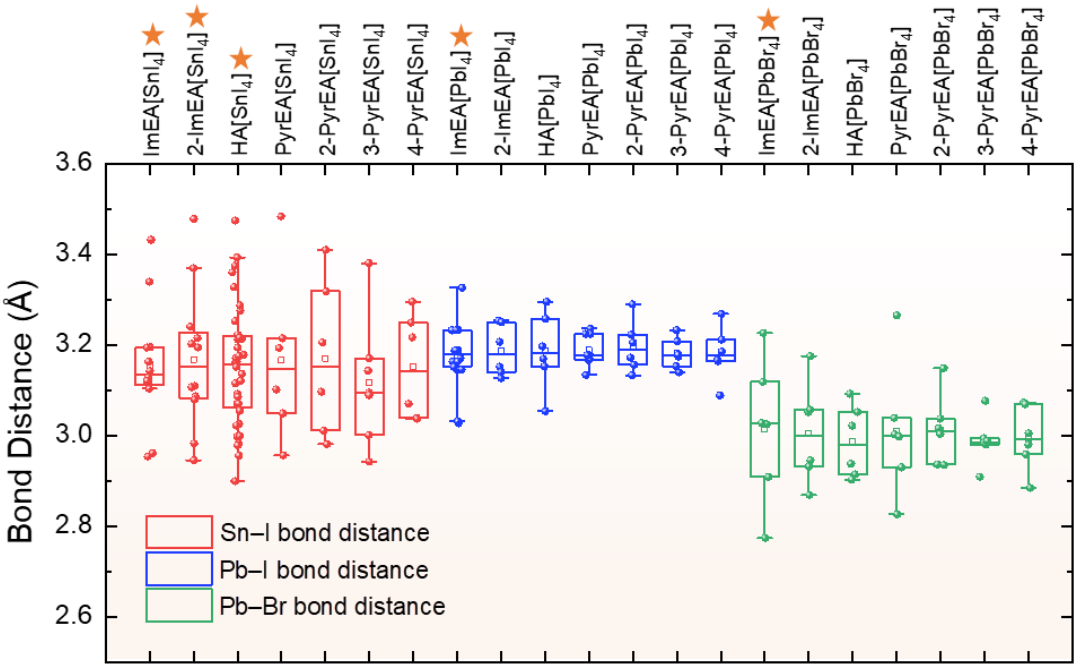

Figure 3. Comparison of the bond length distributions in the 2D Pb-I, Sn-I and Pb-Br perovskites templated by the series of organic dications ImEA, 2-ImEA, HA, PyrEA, 2-PyrEA, 3-PyrEA, and 4-PyrEA. Stars indicate corrugated structures. See **Figure 2** for the molecular structures of the corresponding dications. The depicted bond lengths are listed in **Tables S4-S24**.

Table 1. Off-centre displacements (Å) for 2D group 14 metal halide perovskites, $A[MX_4]$, discussed in this study.[a]

Templating dication, A^{2+}	Off-centre displacement (Å)		
	$A[SnI_4]$	$A[PbI_4]$	$A[PbBr_4]$
$ImEA^{2+}$	0.278	0.297	0.056
$2\text{-}ImEA^{2+}$	0.266	0.153	0.215
HA^{2+}	0.310	0.159	0.166
$PyrEA^{2+}$	0.189	0.059	0.186
$2\text{-}PyrEA^{2+}$	0.196	0.105	0.087
$3\text{-}PyrEA^{2+}$	0.102	0.030	0.078
$4\text{-}PyrEA^{2+}$	0.061	0.041	0.057

[a]The highest value is selected in the case of structures containing multiple geometrically distinct $[MX_6]^{2-}$ octahedra. See **Table S25** for complete list of values.

incorporating the dications studied herein are, in general, much broader than their iodoplumbate congeners. Correspondingly, the displacements of the metal ions from the centroids of the six halides coordinated to them (*i.e.,* the centres of their octahedra) are, on the whole, the largest for the iodostannates and smallest for the iodoplumbates (**Tables 1** and **S25**). The off-centre displacements for the bromoplumbates are intermediate between the two groups of materials. These structural trends are consistent with expectations for stereochemically active metal ns^2 electron pairs, which arise from pseudo- or second-order Jahn-Teller effects.[37-42] This is associated with mixing of metal s and p orbital character (*i.e.,* orbital hybridization), which is mediated by bonding with the halide anions. Relativistic effects render the Pb $6s^2$ electrons less available for overlap with the halide p orbitals than the Sn $5s^2$ electrons. Thus, mixing with the Pb 6p orbitals is comparatively small and, consequently, there are limited structural distortions.[33, 43-45] Similarly, more electronegative anions have better overlap with the metal ns orbitals and leads to them displaying enhanced stereochemical activity.[46-48]

Of the series of iodostannates described in this manuscript, the largest off-center displacements are seen for the Sn centres occupying the ridges of the 3 × 3 (*110*)-oriented lattices (**Table S25**). They range from 0.237 – 0.310 Å, whereas the off-centre displacements in the (*100*) iodostannates range from 0.061 – 0.196 Å. The ridge-occupying octahedra of the (*110*) materials are comprised of two *cis*-oriented terminally bound iodides (I_t), for which the Sn–I bond lengths are unusually short (2.9534(9) and 2.9607(9) Å in $ImEA[SnI_4]$), plus four iodides that bridge (μ-I) to other Sn centres (**Table S4**). The Sn–I distances for the two μ-I *trans* to the I_t are significantly elongated (3.3388(9) and 3.417(9) Å in $ImEA[SnI_4]$). This arrangement is a consequence of the stereochemically active ns^2 pair of electrons being oriented towards the elongated bonds. The metal ions in the (*100*)-oriented compounds tend to display more C_3-symmetric distortions, with three facially-oriented elongated Sn–I bonds. Although the difference in length is often quite severe along one axis (*e.g.,* Sn–I_t in $PyrEA[SnI_4]$ = 2.9558(5) and 3.4835(6) Å; **Table S7**), the distortions are usually much less extreme than the corresponding (*110*) iodostannates.

The general trends in structural distortion described for the iodostannates holds true for their iodoplumbate congeners. In contrast, the Pb^{2+} ions in the (*110*)-oriented compound ImEA[$PbBr_4$] exhibit minimal off-centre displacements of 0.056 Å (**Table S5**). This can be attributed to it possessing 2 × 2 corrugation, rather than the 3 × 3 (or 4 × 4) structures seen in the other (*110*) compounds. In the 2 × 2 corrugated system, the μ-Br halides ions are directly shared between ridge-occupying octahedra, which limits the possible extent of Pb–Br bond elongation/weakening.

It should be noted that regardless of whether they possess (*110*)- or (*100*)-oriented structures, the metal halide lattices accompanying imidazole-based templating dications $ImEA^{2+}$, 2-$ImEA^{2+}$ and HA^{2+} generally display greater structural distortions than their pyridine-based dication templated analogues. This is a result of the earlier discussed supramolecular interactions between the organic and inorganic components and is a testament to their importance in controlling the micro-structure of the lattice. We postulate that once the level of distortion reaches a certain threshold, the (*110*)-oriented lattices become favored relative to (*100*) structures. In the case of iodoplumbates and bromoplumbates, this is seen only for $ImEA^{2+}$. As the $5s^2$ electrons of stannates are more stereochemically active than the $6s^2$ electrons of plumbates, the threshold is more easily passed and (*110*)-oriented lattices are obtained for a wider array of templating cations. In other words, we would expect (*110*)-oriented 2D structures to be more common for stannates than plumbates. Furthermore, it is likely that more electronegative halides will further enhance or exaggerate this effect.

NMR spectra of (*110*)- *vs* (*100*)-oriented structures. The difference between the coordination environments of Sn in ImEA[SnI_4] and the (*100*)-oriented 2D iodostannates, exemplified here by 3-PyrEA[SnI_4] (3-$PyrEA^{2+}$ = 3-(2-ammonioethyl)pyridin-1-ium), can be discerned in powdered samples using static solid-state NMR (SSNMR) measurements. In particular, the static ^{119}Sn SSNMR spectrum of 3-PyrEA[SnI_4] contains a single resonance at -135 ppm, whereas that of ImEA[SnI_4] contains two overlapping peaks (**Figures 4a-b**). Gaussian fitting of the latter allows deconvolution into two resonances of equal intensity, centred at -23 and -327 ppm. These observations are in accordance with the X-ray crystal structures of these compounds. As with all (*100*)-oriented structures, 3-PyrEA[SnI_4] contains only a single type of Sn coordination environment. In other words, all of the Sn ions are equivalent. However, the Sn ions in ImEA[SnI_4] alternate across a sheet (along the b and c axes) between having two terminally-bound iodide ions *cis* and *trans* to one another. These arrangements correspond to Sn ions at the vertices and those on the flat slopes between them, respectively.

Variations in the environments of the organic countercations in ImEA[SnI_4] and 3-PyrEA[SnI_4] are also apparent in their magic angle spinning (MAS) ^{13}C SSNMR spectra (**Figures 4c-d**). Each chemically distinct carbon atom in 3-$PyrEA^{2+}$ yields a single resonance, but peaks indicative of two inequivalent dications are observed for $ImEA^{2+}$ (*i.e.*, double the number). This is consistent with the numbers of distinct dications in the X-ray structures of their respective iodostannates (**Figure S5**).

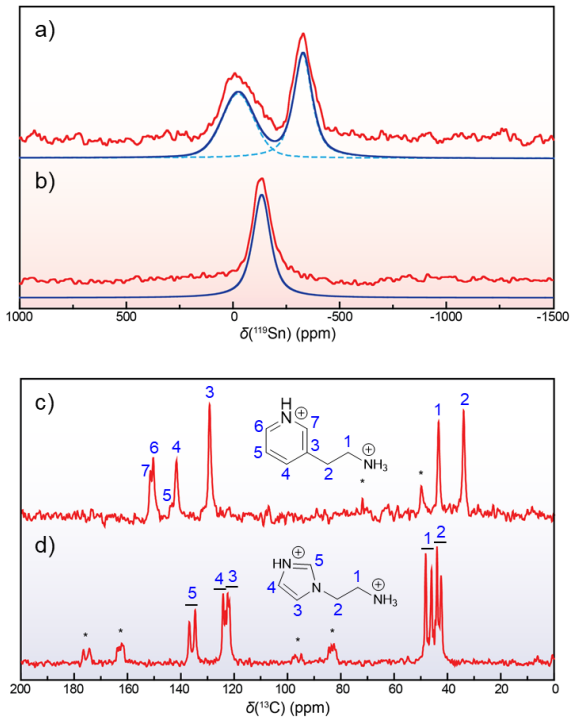

Figure 4. Room temperature, static ^{119}Sn solid-state (SS) NMR spectra of a) "3 × 3" (*110*)-oriented ImEA[SnI_4] and b) (*100*)-oriented 3-PyrEA[SnI_4]. Experimental data, total simulated line-shapes, and deconvoluted simulated resonances are depicted using red, blue and dashed sky blue lines, respectively. Room temperature magic angle spinning (MAS) ^{13}C SSNMR spectra of c) 3-PyrEA[SnI_4] and d) ImEA[SnI_4].

Photophysical properties of ImEA[SnI_4]. Previously, it has been demonstrated that interlayer separation in *n* = 1 2D perovskites plays a critical role in determining photocurrent generation in the corresponding solar cell devices. In particular, short perpendicular contacts favour superior charge transport.[35, 49] As a consequence, the photophysical properties of ImEA[SnI_4] were further investigated to assess its suitability for photovoltaic applications. The UV-Vis absorption spectrum of ImEA[SnI_4] is presented in **Figure 5a** (blue curve) and, in analogy to other *n* = 1 2D iodostannates, [27, 50] the band centred at ~580 nm can be attributed to excitonic absorptions of the tin iodide lattice. As observed for *n* =*1* 2D iodoplumbates, the excitonic transition of ImEA[SnI_4] is blue-shifted relative to those of (*100*)-oriented 2D tin iodide perovskites, which range from 600 nm to 700 nm.[21, 27] This can be attributed to poorer Sn 5s and I 5p orbital overlap in the corrugated sheets relative to (*100*) oriented structures.[26, 51-52] Nonetheless, the excitonic transition of ImEA[SnI_4] is, of course, bathochromically-shifted with respect to that of the corresponding isostructural Pb compound ImEA[PbI_4].[26] The lower band gap in the Sn compound, that this equates to, is a consequence of the lower electronegativity and smaller size of

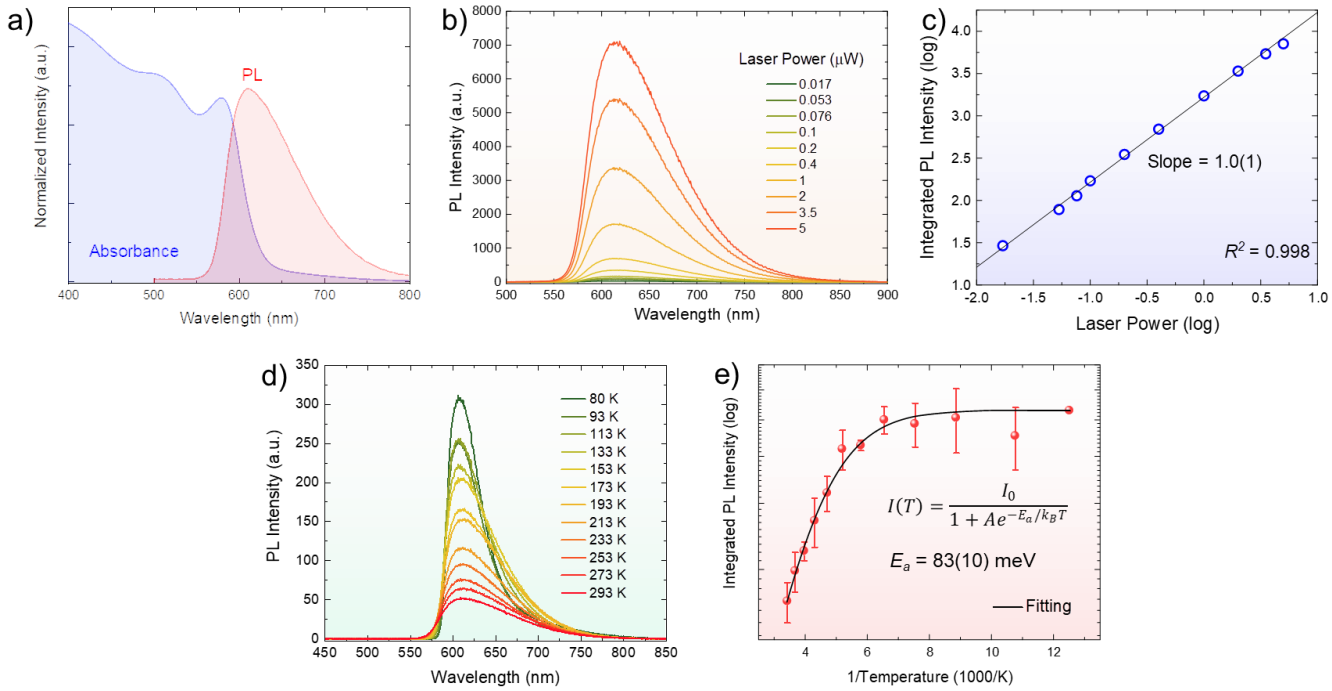

Figure 5. a) Room temperature UV-visible absorbance and photoluminescence (PL) spectra of ImEA[SnI_4]. b) Evolution of the photoluminescence spectrum of ImEA[SnI_4] as a function of laser power, at 293 K excited by 573 nm wavelength. c) Plot and linear fit of the dependence of photoluminescence intensity of ImEA[SnI_4] *versus* laser power, monitored at 611 nm wavelength, measured in the range 0.017 – 5 μW, at 293 K. d) Temperature-dependent photoluminescence (PL) spectra of single crystal ImEA[SnI_4], recorded using a 573 nm continuous-wave laser beam. d) Temperature-dependent integrated PL intensity of single crystal ImEA[SnI_4]. The solid line is a best fit of the experimental data (red circles) to the Arrhenius equation, where I_o corresponds to the intensity at 0 K, E_a to the activation energy, and k_B to the Boltzmann constant.

Sn^{2+} relative to Pb^{2+}.[53-55] This is consistent with the DFT calculated optical absorption spectra (**Figure S6**) and total density of states (**Figure S7**) of ImEA[SnI_4] and ImEA[PbI_4], wherein the former exhibits extended visible light absorption and a lower band gap compared with the latter.

Room temperature excitation of ImEA[SnI_4] at 573 nm yields a photoluminescence (PL) emission spectrum containing a moderately intense, asymmetric peak at 611 nm, with a full width at half maximum (fwhm) of *ca.* 95 nm (300 meV), and a Stokes shift of *ca.* 109 meV (Figure 3a, red curve). As shown in **Figure S8**, the CIE coordinates of the emission are (0.64, 0.36), which corresponds to red light emission. As might be anticipated for a (*110*)-oriented inorganic lattice, the observed PL signature is broader than seen for conventional (*100*)-oriented congeners. For instance, BA- and PEA-based tin iodide perovskites exhibit PL peaks with fwhm of less than 40 nm.[56-57] In the case of Pb-based materials, these trends in emissive behaviour have been hypothesized to arise from self-trapped excitons (STEs), with the greater fwhm and Stokes shift values in the more distorted (*110*) structures being a consequence of enhanced exciton-phonon coupling.[51, 58] (See **Table S26** and accompanying text for detailed analysis of the structural distortions of ImEA[SnI_4] and selected Sn-I compounds.) When ImEA[SnI_4] is excited with laser power ranging from 0.017 to 5 μW, PL intensity increases linearly and shows no signs of saturation (**Figures 5b-c**). This supports the notion that emission arises from STEs and not from permanent defects.

The good visible light absorption capability of ImEA[SnI_4], which spans up to 650 nm, prompted us to study the behaviour of its photogenerated charge carriers. To that end, we performed temperature-dependent PL measurements between 80 and 293 K. The resulting spectra are presented in **Figure 5d**, while the PL spectra with normalized emission intensities appear in **Figure S9**. Plotting emission intensity against the inverse of temperature and fitting the data to the Arrhenius equation (**Figure 5e**) provides an estimated activation energy (E_a) of 83(10) meV. Very few E_a's have been reported for n = 1 2D iodostannates, which would seemingly limit the context available for this value. However, the aforementioned value is essentially identical to the E_a of *ca.* 94 meV previously measured for its lead analogue ImEA[PbI_4].[26] The same can also be said for $(PEA)_2[SnI_4]$ and $(PEA)_2[PbI_4]$, which have respective E_a's of *ca.* 190[59] and 220 meV,[60] and 3D Sn-I and Pb-I perovskites (E_a values ranging from 10 to 20 meV).[55, 61] Given that n = 1 2D iodoplumbates templated by alkyl ammonium cations typically have E_a values above 300 meV, while those of more polarizable aromatic cations are around 200 meV,[60, 62] it can be inferred that the E_a measured for ImEA[SnI_4] is likely to be much lower than the expected for a typical Sn-based n = 1 2D perovskite. We believe that

this stems from ImEA[SnI_4] possessing a combination of very short Sn-I layer separations and relatively highly polarizable aromatic dications. These factors, effectively, render the perovskite more "3D-like" in character.

DFT calculations. To obtain further insight into the electronic structure of ImEA[SnI_4] and how it compares with that of ImEA[PbI_4], we performed density functional theory (DFT) calculations. The total and projected density of states (DOS and PDOS, respectively) for these two compounds are given in **Figures 6** and **S7**, respectively. The accuracy of the electronic structures obtained is evidenced by the acceptable agreement between their respective DFT simulated (**Figure S6**) and experimentally measured UV-Vis spectra. As seen in other Sn-based 2D perovskites,[49] the primary contributor to the valence band maximum (VBM) in ImEA[SnI_4] are antibonding combinations of the Sn $5s^2$ and I 5p orbitals, with the latter being dominant. From the projected density of states, it is clear that orbital mixing introduces Sn 5p character into this interaction. This equates to orbital hybridization and results in stereochemical activity of the Sn $5s^2$ lone pair. The near edge of the valence band is comprised mostly of fully occupied non-bonding I 5p orbitals (*ca.* -1.5 eV) and below that there are bonding overlaps between the 5p orbitals of iodide and Sn (*ca.* -3 eV). The anti-bonding components of the latter,

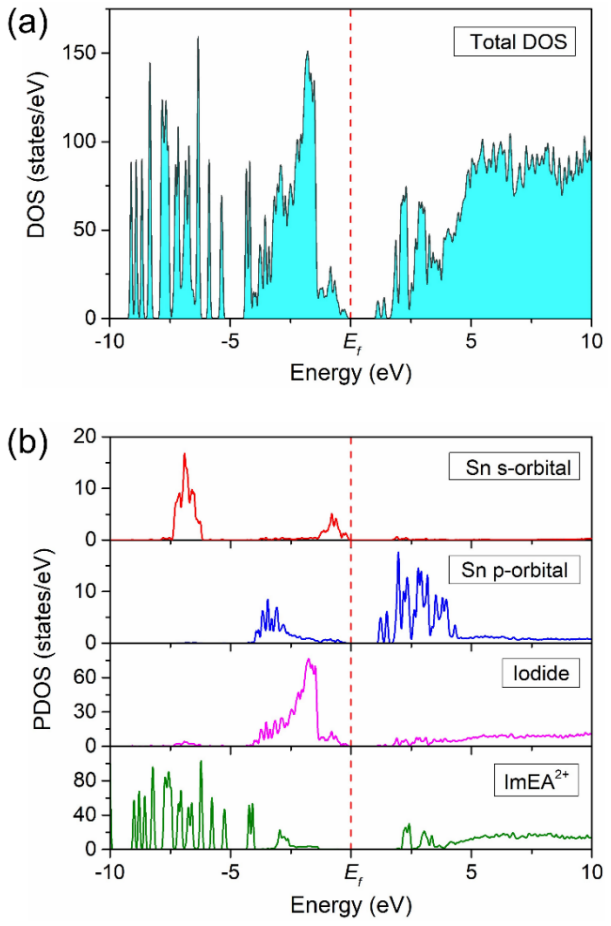

Figure 6. DFT calculated a) total density of states (DOS) and b) projected density of states (PDOS) for ImEA[SnI_4], where E_f corresponds to the Fermi level.

which are metal dominated, are the primary contributors to the conduction band minimum (CBM).

The PDOS for the Pb compound ImEA[PbI_4] has similar features to that of ImEA[SnI_4], but there are key differences. Although the antibonding components of the interactions between the Pb $6s^2$ and I 5p orbitals do appear at the valence band maximum, they are not well separated from the non-bonding I 5p orbitals (*ca.* -0.8 eV). In contrast, the separation is clear and comparatively large in the Sn compound. This contributes to the smaller band gap of ImEA[SnI_4] and reflects the greater availability of the Sn $5s^2$ electrons for bonding, relative to the Pb $6s^2$ electrons, which is a consequence of the comparatively low energy of the latter. In other words, the inert pair effect. A further consequence of the greater overlap with the I 5p orbitals is that the Sn $5s^2$ electrons would be expected to be more stereochemically active than the Pb $6s^2$ lone pairs. This assertion is borne out by X-ray structure discussion above.

Interestingly, the near-edge regions of the conduction bands of both ImEA[SnI_4] and ImEA[PbI_4] feature significant contributions from the conjugated aromatic dication $ImEA^{2+}$. This raises the possibility of charge transfer from the inorganic to the organic components of these materials and might be expected to endow them with enhanced inter-layer conductivity. Interactions of this type, which led to similar inferences, have precedence in one-dimensional (1D) lead iodide hybrids containing the electron deficient aromatic tropylium[63] and viologen[64] templating cations.

Lead-free 2D perovskite solar cell application. The low E_a measured for ImEA[SnI_4] signifies that separation of its photogenerated charge carriers proceeds with comparative ease. In response, 2D perovskite solar cells adopting the inverted *p-i-n* architecture were fabricated (**Figure 7a**; see SI for further details). More specifically, devices consisting of a stack of indium tin oxide (ITO)/poly(3,4-ethylenedioxythiophene): poly(styrene-sulfonate) (PEDOT:PSS, 40 nm)/ImEA[SnI_4] (400 nm)/[6,6]-phenyl-C_{61}-butyric acid methyl ester (PCBM, 30 nm)/ bathocuproine (BCP, 7 nm)/aluminium (Al, 100 nm) was chosen in our study. This configuration was selected because the dopants present in commonly employed hole transporting materials (HTM), such as Spiro-OMeTAD, were found to accelerate the deterioration of tin perovskites. Additionally, the HTM energy levels in *n-i-p* devices are, generally, not aligned with those of n = 1 2D tin iodide perovskites.[9, 27, 65-66] In contrast, as shown in **Figure 7b**, the band energies of ImEA[SnI4] align well with those of the electron/hole transporting layers in inverted devices. In particular, the conduction band edge of ImEA[SnI_4] is determined *via* ultraviolet photoelectron spectroscopy (UPS) to be -5.2 eV (**Figure 7b**), while the band gap is estimated to be *ca.* 2.02 eV (**Figure S10**). The HOMO of PEDOT:PSS and LUMO of PCBM are known to be *ca.* -5.0 eV and -4.2 eV, respectively.[67-69] This good alignment promotes efficient interfacial charge transfer in the perovskite solar cell devices. Scanning electron microscopy (SEM) and atomic force microscopy (AFM) images confirm the compactness and smoothness of the perovskite layer (**Figures S11 and S12**,

respectively), while its crystallinity was established with glancing-angle X-ray diffraction (GAXRD; **Figure S13**).

The optimized precursor concentration for spin-coating solutions of ImEA[SnI_4], in 7:3 mixtures of DMF and DMSO, was found to be 0.75 M. Details of concentration-dependent device performance parameters, average device performances, and corresponding characterization data can be found in **Tables S27-S29**. Additionally, statistical representations of individual photovoltaic parameters of 10 devices, based on ImEA[SnI_4], which confirm the reproducibility of the device fabrication process, are depicted in **Figures 7c** and **S14a-d,** and summarized in **Table S28**. Meanwhile, current density-voltage (*J-V)* characteristics of the best device fabricated from ImEA[SnI_4] are presented in **Figure 7d** and **Table 2**.

Table 2. Selected photovoltaic parameters of the best performing device based on ImEA[SnI_4].[a]

Scan direction	V_{oc} (mV)	J_{sc} (mA cm^{-2})	FF (%)	PCE (%)
Reverse	446	9.12	55.62	2.26
Forward	431	9.12	56.19	2.21

[a]V_{oc}, J_{sc}, FF, PCE correspond to open-circuit voltage, short-circuit current density, fill-factor, and power conversion efficiency, respectively.

In our devices, the forward scan of current as a function of potential, under 1 sun white light irradiation, was found to be almost identical with the reverse scan (**Figure 7d, Table 2**). This lack of hysteresis is indicative of minimal ion migration within ImEA[SnI_4], which can be attributed to the bulky and dicationic nature of $ImEA^{2+}$.[20, 70] This conclusion is supported by poling measurements conducted on thin-film lateral devices featuring interdigitated electrodes (see **Figure S15** and SI for details). Therein, application of a pulsed field of 2 V μm^{-1} (**Figure S16**) induces an open circuit voltage inside the material of about 200 mV (**Figure S17**). This resembles the switchable photovoltaic behavior reported for 3D lead halide perovskites, in which an intrinsic *p-n* junction is born from the charge imbalance created by ion migration. However, this effect is less reversible in ImEA[SnI_4] than it is for 3D lead halide perovskites,[71] a fact that can be attributed to slower migration of the organic cations in the former due to their larger size and greater charge.[20, 70]

The best performing PV cell based on ImEA[SnI_4] supplied a short-circuit current density (J_{sc}) as high as 9.12 mA cm^{-2}. This represents a more than two-fold improvement over the overwhelming majority of Pb-based n = 1 2D perovskite solar cells.[18-19, 26, 72-73] This includes its Pb-based counterpart ImEA[PbI_4] (J_{sc} = 3.94 mA cm^{-2}) and the best performing PV device utilizing a pure n = 1 2D solar absorber documented thus far, which contains (3-APN)$_2$[PbI_4], has a PCE of 3.39 %, and a J_{sc} of only 5.73 mA cm^{-2}.[19] Such superior charge collection in ImEA[SnI_4], relative to Pb-based n = 1 2D perovskites, is primarily due to the better visible light absorption capabilities of iodostannates. As shown in the incident photon-to-current efficiency (IPCE) spectrum of the best performing device (**Figure 7e**), the device absorption onset extends to 650 nm, which correlates with the UV-Vis absorption band edge of the material. In contrast, Pb-based n = 1 2D perovskite solar cells typically feature absorption onsets < 600 nm.[18-19, 26, 72-73]

An additional likely contributor to the comparatively high efficiency of current generation in our devices is the low exciton activation energy in ImEA[SnI_4]. As mentioned above, this is believed to be associated with the very short separation between the inorganic layers of the material and the polarizability of the aromatic templating cations, $ImEA^{2+}$. This is reflected by IPCE values of up to 70 %. For comparison, a value of 65 % was reported for a device based on Bn_2[SnI_4], which features larger iodostannate sheet spacing (I···I closest contacts of 8.077 Å).[27] Thus, our results indicate that modulation of the distance between the inorganic layers can play a pivotal role in further mitigating the efficiency limits of 2D metal halide perovskites. When coupled with a good open-circuit voltage (V_{oc}) of over 400 mV and a fill-factor of 55 %, the best performing PV device containing ImEA[SnI_4] displayed a PCE of 2.26 %. (See **Figure 7c** for the histogram of device PCEs.) This value is nearly identical to that of the only other reported n = 1 2D Sn-based perovskite solar cell (2.35 %), and makes our device one of the most efficient fabricated from n = 1 2D group 14 metal halide perovskites.[18, 26-27, 72]

Table 3. Photovoltaic performances of best performing pure 2D perovskite solar cells.

Compound	Device architecture	PCE
Bn_2[SnI_4]$^{\alpha}$	FTO/c-TiO_2/meso-TiO_2/2D PVK/Au	2.35 %
ImEA[SnI_4]$^{\beta}$	ITO/PEDOT:PSS/2D PVK/PCBM/BCP/Al	2.26 %*
BdA[PbI_4]$^{\gamma}$	FTO/c-TiO_2/meso-TiO_2/2D PVK/ Spiro-OMeTAD/Ag	1.08 %
HA[PbI_4]$^{\delta}$	ITO/PEDOT:PSS/2D PVK/PCBM/Al	1.13 %
(POPA)$_2$[PbI_4]$^{\varepsilon}$	ITO/PEDOT:PSS/2D PVK/Ag	1.38 %
ImEA[PbI_4]$^{\beta}$	FTO/c-TiO_2/meso-TiO_2/2D PVK/ Spiro-OMeTAD/Au	1.83 %
(3-APN)$_2$[PbI_4]$^{\zeta}$	ITO/NiOx/2D PVK/PCBM/Ag	3.39%

$^{\alpha}$benzimidazolium,[27] $^{\beta}$1-(2-ammonioethyl)-1H-imidazol-3-ium,[26] $^{\gamma}$Butane-1,4-diaminium,[73] $^{\delta}$histammonium,[29] $^{\varepsilon}$3-(pyren-2-yloxy) propan-1-aminium,[18] $^{\zeta}$2-cyanoethan-1-aminium,[19] *This work.

CONCLUSIONS

In conclusion, we have disclosed the two examples of "3 × 3" (*110*)-oriented n = 1 2D tin iodide perovskites. Isomeric imidazolium-based dications were used to template these

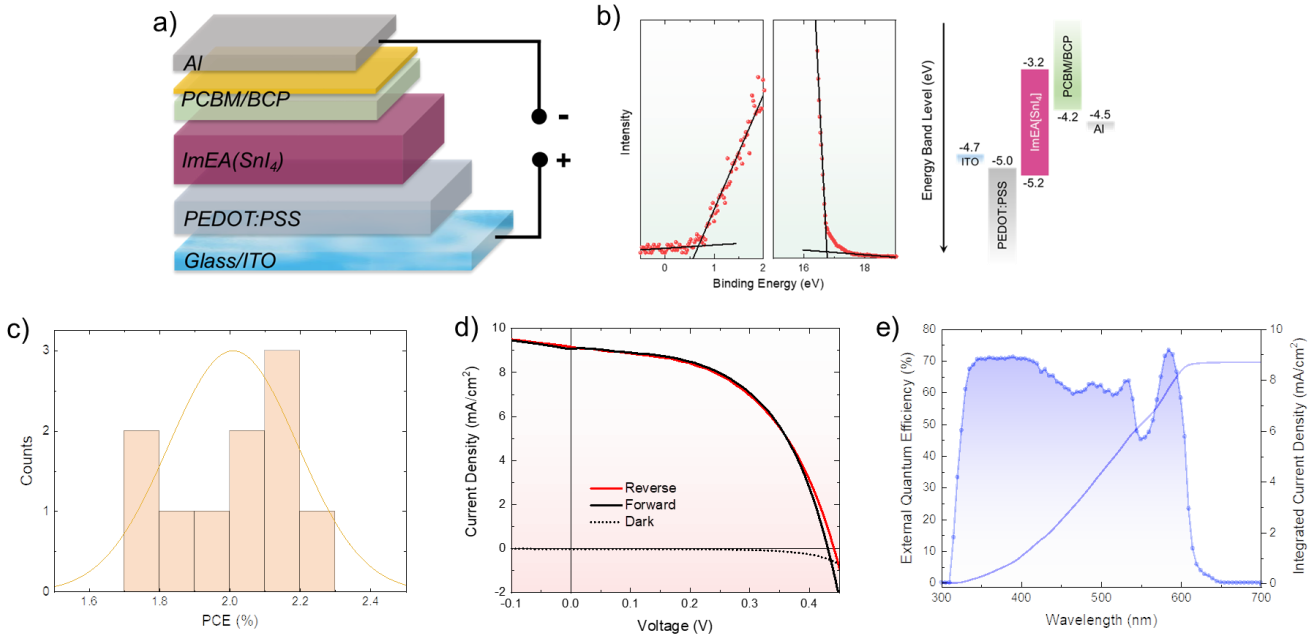

Figure 7. a) Schematic representation of the perovskite solar cell configuration employed in this study. b) Ultraviolet photoelectron spectroscopy (UPS) spectrum of a thin film of ImEA[SnI_4], plus a band energy diagram of the solar cell that is comprised of ImEA[SnI_4], the charge transport materials, and the electrodes. Extrapolation of the spectral offset allows estimation of the material's valence band energy level, and the band gap was extracted from the Tauc Plot of the thin film's absorption spectrum (**Figure S10**). c) Statistical representations of power conversion efficiency (η) measured for 10 photovoltaic devices containing the solar absorber ImEA[SnI_4]. d) Photovoltaic current density-voltage (J–V) characteristics of the best performing solar cell fabricated using ImEA[SnI_4] as the solar absorber, under white light irradiation (1 sun; AM 1.5 G). e) External quantum efficiency (EQE) spectrum of the best performing solar cell, which displays an integrated short-circuit current density (J_{sc}) of 8.65 mA cm^{-2}.

materials. The presence of two endocyclic N-atoms in the imidazolium core, both of which have supramolecular interactions with the tin iodide framework, plays a pivotal role in inducing formation of the corrugated structure. This is deduced from the observation of more common (*100*)-type 2D perovskite structures for templating dications containing pyridinium cores, irrespective of the position of the 2-ethylammonium substituent. In addition, the higher tendency of the $5s^2$ lone pairs of Sn^{2+} ions to express stereoactivity relative to the $6s^2$ electrons of Pb^{2+} renders the corresponding iodostannate lattice more prone to corrugation. This is inferred from the broader distribution of metal halide bond distances and the larger off-center displacements relative to their 2D haloplumbate congeners.

The very short inorganic layer separation in ImEA[SnI_4] (I···I contacts as small as 4.174 Å), as a consequence of the compactness of the dication, combines with the polarizable nature of the imidazolium moiety to yield an exciton activation energy (E_a) as low as 83(10) meV. When used as a solar absorber, these features allow harvest of short-circuit current densities (J_{sc}) of more than 9 mA cm^{-2}. Superior charge collection in ImEA[SnI_4], compared to n = 1 2D Pb-halide perovskites, is attributed to its comparatively low energy light absorption onset of *ca.* 650 nm. In addition, relative to previously reported solar cells based on $Bn_2[SnI_4]$ (I···I contacts of 8.077 Å), better IPCE conversions of up to 70 % were obtained from ImEA[SnI_4], which is attributed to the shorter inorganic layer separation in the latter. This allows access to photovoltaic cells with power conversion efficiencies of 2.26 %, which is amongst the highest values reported, so far, for n = 1 2D metal halide perovskite solar cells (Table 3).

Thus, this work contributes substantially to the field of low-dimensional perovskites in two respects. Firstly, the impact of systematic tuning of the templating organic cation upon inorganic architecture detailed herein provides insight into the factors (*i.e.,* secondary intermolecular interactions and stereochemical activity of s orbital electron lone pairs) that induce 2D hybrid perovskites featuring specific inorganic lattice fine structures. Secondly, we have provided only the second example of a PV device that employs a n = 1 2D tin halide perovskite as a solar absorber and shown that it displays an efficiency superior to all, but one, of the many examples of n = 1 2D Pb-based materials. Given that the improved performance of the iodostannate is tied to its inherently greater light absorption capabilities, we would argue that these materials have greater potential than their more toxic Pb-based congeners. The highly malleable nature of the iodostannate lattice means that molecular design of templating organic cations will be crucial in this process, with inorganic layer separation and intra- and

inter-octahedral distortions being particularly important factors in tailoring their optoelectronic performance.

EXPERIMENTAL SECTION

Materials synthesis

Chemicals. Aqueous hydroiodic acid (57 wt. %, distilled, 99.999%), tin(II) iodide (–10 mesh, 99.999%), tin(II) fluoride (99%), 2-(1*H*-imidazol-4-yl)ethan-1-amine hydrochloride (95%), 2-(pyridin-2-yl)ethan-1-amine (95%), 2-(pyridin-3-yl)ethan-1-amine (95%), 2-(pyridin-4-yl)ethan-1-amine (96%), and tin powder (≥99%) were obtained from Sigma-Aldrich. Pyridine (HPLC Grade, >99.5%) and ethanolamine (>99%) were bought from Alfa Aesar. 2-(1*H*-Imidazol-1-yl)ethan-1-amine (95%) and 2-(1*H*-imidazol-2-yl)ethan-1-amine hydrochloride (95%) were purchased from Fluorochem and Combi-Blocks, respectively. Poly(3,4-ethylenedioxythiophene):poly(styrene-sulfonate) (PEDOT:PSS), [6,6]-phenyl-C_{61}-butyric acid methyl ester (PCBM; 99.95%) and bathocuproine (BCP; Sublimed, > 99% (HPLC)) were obtained from Clevios Al4083, Solenne BV, and Lumtec, respectively. Unless otherwise stated, all reagents were used without purification. Anhydrous diethyl ether, dimethylformamide (DMF) and dimethyl sulfoxide (DMSO) were obtained from Sigma-Aldrich, and thoroughly degassed prior to use *via* the freeze-pump-thaw method. The salts 2-iodoethan-1-ammonium iodide, 1-(2-ammonioethyl)pyridin-1-ium diiodide ($PyrEA(I)_2$), and 1-(2-Ammonioethyl)-1*H*-imidazol-3-ium diiodide ($ImEA(I)_2$), were synthesized *via* previously reported procedures.[26]

General procedure used to synthesize the remaining ammonium iodide salts. A stoichiometric amount of concentrated hydroiodic acid was added to an ice cooled round-bottom flask containing ethanol and the requisite amine. After stirring the resulting mixture for 1 hour, all volatiles were removed using a rotary evaporator. The solids, thereby, obtained were washed with copious amounts of diethyl ether and dried under vacuum, overnight, at 50 °C.

2-(2-Ammonioethyl)pyridin-1-ium diiodide, 2-PyrEA(I)$_2$. Isolated as a beige powder (1.61 g, 85 % yield). ^{1}H NMR (400 MHz, DMSO-d_6): δ 8.88 (d, 1 H, ArH), 8.50 (t, 1 H, ArH), 8.13 (bs, 3 H, NH_3^+), 7.99 (d, 1 H, ArH), 7.92 (t, 1 H, ArH), 3.39-3.32 (m, 4 H, CH_2). ^{13}C{^{1}H} NMR (100 MHz, DMSO-d_6): δ 152.7, 145.4, 142.7, 127.2, 125.2, 37.3, 31.0.

3-(2-Ammonioethyl)pyridin-1-ium diiodide, 3-PyrEA(I)$_2$. Isolated as a beige powder (0.84 g, 92 % yield). ^{1}H NMR (400 MHz, DMSO-d_6): δ 8.92 (s, 1 H, ArH), 8.86 (d, 1 H, ArH), 8.53 (d, 1 H, ArH), 8.04 (t, 2 H, ArH), 7.98 (bs, 3 H, NH_3^+), 3.23-3.20 (m, 2 H, CH_2), 3.16-3.12 (m, 2 H, CH_2). ^{13}C{^{1}H} NMR (100 MHz, DMSO-d_6): δ 146.3, 142.5, 140.7, 137.1, 126.8, 38.8, 29.6.

4-(2-Ammonioethyl)pyridin-1-ium diiodide, 4-PyrEA(I)$_2$. Isolated as a beige powder (1.20 g, 83 % yield). ^{1}H NMR (400 MHz, DMSO-d_6): δ 8.92 (d, 2 H, ArH), 8.05 (bs, 3 H, NH_3^+), 8.04 (d, 2 H, ArH), 3.25-3.20 (m, 4 H, CH_2). ^{13}C{^{1}H} NMR (100 MHz, DMSO-d_6): δ 157.9, 141.7, 127.6, 38.1, 32.6.

Growth of single crystals of hybrid perovskites. In general, stoichiometric amounts of SnI_2 and organic iodide salt, were added to sufficient concentrated aqueous HI (stabilized through addition of 5 % H_3PO_2, v/v relative to HI, and degassed prior to use) to give 0.25 – 0.30 M concentrations of Sn^{2+}. The resulting mixtures were heated, with stirring, under an Ar atmosphere, at ~120 °C for approximately 30 mins until clear solutions were obtained. Subsequent *slow* cooling to room temperature afforded single crystals suitable for X-ray crystallography. The single crystals were then isolated under an Ar atmosphere, using a filter stick connected to a Schlenk line, washed with degassed anhydrous diethyl ether, and transferred to an inert atmosphere glovebox for storage and handling.

Thin film fabrication. Thin films used in characterization of the optical properties of the compounds were prepared by adaptation of previously published procedures, involving Sn metal and SnF_2 additives.[4, 74-75] Typically, 0.75 M solutions of stoichiometric amounts of SnI_2 and $ImEA(I)_2$, containing SnF_2 (10 mol %, relative to SnI_2) and Sn (10 mg mL^{-1}) additives, dissolved in a 7:3 mixture of DMF and DMSO, were filtered and spin coated, at 4000 rpm for 30 s, onto pre-cleaned glass or FTO-patterned (100 μm spaced) substrates. (The substrates were pre-cleaned by sequential sonication for 15 min periods each in soap solution (Decon), deionized water, acetone, ethanol, and isopropanol, followed by ozone plasma treatment for 15 mins.) In order to remove residual solvents, the resulting films were heated at 120 °C for 15 mins.

Solar cell device fabrication. Pre-etched indium tin oxide (ITO) glass substrates (sheet resis- tance of 8 Ω cm^{-1}) were washed by sonication consecutively in Hellmanex detergent solution (2% v/v in deionized water), deionized water, acetone, ethanol, and isopropanol. The cleaned substrates were then dried and treated for 15 mins with ozone plasma. Subsequently, poly(3,4-ethylenedioxythiophene):poly(styrene-sulfonate) (PEDOT:PSS) aqueous solution was filtered through a 0.45 μm PVDF syringe filter and spin coated for 1 min at 4000 rpm (acceleration of 200 rpm s^{-1}) onto the substrate, after which it was thermally annealed for 20 mins at 130 °C to remove any residual solvent. The substrates were then transferred into an argon-filled glovebox (O_2 and H_2O < 0.1 ppm) for the remainder of the fabrication processes.

Solutions comprised of a range of concentrations (0.50, 0.75 and 1.00 M) of stoichiometric amounts of SnI_2 and $ImEA(I)_2$, plus SnF_2 (10 mol%, relative to SnI_2) and Sn (10 mg/mL) additives, dissolved in thoroughly degassed 7:3 mixtures of DMF and DMSO, were filtered and spin coated for 30 s at 4000 rpm (acceleration of 2000 rpm s^{-1}) onto the PEDOT:PSS coated substrate. After annealing at 120 °C for 15 mins (and allowing to cool), a layer of [6,6]-phenyl-C_{61}-butyric acid methyl ester (PCBM, 20 mg mL^{-1} in chlorobenzene) was dynamically spin coated onto the perovskite film at 2000 rpm for 30 s. This was followed by annealing at 100 °C for 10 mins. Once cooled to room temperature, a very thin layer of bathocuproine (BCP, 0.5 mg mL^{-1} in ethanol) was then added by dynamic spin coating at 4000 rpm for 20 s. Finally, an aluminium electrode (thickness of *ca.* 100

nm) was carefully thermally evaporated onto the BCP layer, under high vacuum (10^{-6} Torr), through a metal shadow mask. The active area of all devices used herein was 0.04 cm^2. All solar cell devices were encapsulated in epoxy resin before being taken out from the Ar-filled glovebox for further characterization, under ambient conditions (70 % RH). Typically, measurements were carried out on the same day the devices were fabricated.

It was observed that even with the encapsulation technique employed (UV-cured resin (LT-U001, LumTec), plus glass cover slide on top of the solar cells stack), the resulting devices experience a significant decrease in terms of efficiency (devices drop typically to around 50 % of initial efficiency, with some of them were found to become non-working) upon storage under ambient conditions (RT; 70 % RH) for only 1 – 2 days. The performance drop occurs despite the physical appearance of the active layer remaining largely unchanged, suggesting that oxidation of small amounts of Sn^{2+} to Sn^{4+} alter the overall electronic properties of the materials. We believe that these instability issues can be greatly mitigated *via* development of better packaging or encapsulation methods, coupled with surface passivation by polymeric species, which could minimize ingress of oxygen into the perovskite layers.

Instrumentation and methods

Nuclear Magnetic Resonance (NMR) spectroscopy. ^1H and $^{13}C\{^1H\}$ NMR spectra of the organic compounds were recorded, in DMSO-d_6 solution, using a Bruker Avance 400 MHz spectrometer. Chemical shift values (ppm) are referenced against residual protic solvent peaks. All solid state (SS) NMR experiments were undertaken using a Bruker Avance III HD 600 MHz spectrometer, with a Bruker 4 mm HXY MAS probe. The ImEA[SnI_4] sample was found to be conductive and, to avoid associated detuning effects, it was mixed with a powdered insulator (50 wt% MgO) in the NMR sample rotor. Simulation of the SS NMR spectra was performed using *dmfit*.[76]

The SS ^{119}Sn NMR experiments were completed at 14.1 T (υ_0 (^{119}Sn) = 223.81 MHz), under static conditions, and the resulting data referenced against $SnO_{2(s)}$ (δ_{iso} = –604.3 ppm). A ^{119}Sn $\pi/2$ pulse length of 4 μs, determined for $SnO_{2(s)}$, was utilised throughout. A one-pulse experiment was employed for 3-PyrEA[SnI_4], whereas a VOCS Hahn-echo sequence was required to uniformly excite the wider line-shape of ImEA[SnI_4].[77] Recycle delays of 1 s and 30 s were used for the ImEA[SnI_4] and 3-PyrEA[SnI_4] samples, respectively. The significantly faster relaxation observed in the ImEA[SnI_4] sample is attributed to its conductive nature.

The SS ^{13}C NMR experiments were completed at 14.1 T (υ_0 (^{13}C) = 150.92 MHz), with MAS frequencies of 6 and 12 KHz used for ImEA[SnI_4] and 3-PyrEA[SnI_4], respectively. (A lower spinning speed was used for the former sample in order to reduce spectral overlap of the ^{13}C resonances and neighbouring spinning sidebands.) The resulting data was referenced against adamantane ($C_{10}H_{16(s)}$; δ_{iso} = 38.48, 40.49 ppm). A ^{13}C CPMAS pulse sequence utilising a ^1H $\pi/2$ pulse length of 2.3 μs (determined for adamantane), a contact pulse length of 4000 μs, a recycle delay of 30 s, and high-power proton decoupling were employed throughout.

UV-vis spectroscopy, field emission scanning electron microscopy (FESEM), atomic force microscopy (AFM), X-ray photoelectron spectroscopy (XPS), and ultraviolet photoelectron spectroscopy (UPS). UV-vis absorption spectra were recorded in the wavelength range 300 – 800 nm, using a SHIMADZU UV-3600 spectrophotometer, with an integrating sphere (ISR-3100). Surface morphology images of the 2D perovskite thin films used in the photoresponse studies were recorded using a JEOL JSM-7600F field emission scanning electron microscope (FESEM), with an accelerating voltage of 5 kV. AFM measurements were conducted using a Bruker Icon microscope; all measurements were performed in the standard tapping mode, using OTESPA-R3 tips from Bruker.

XPS studies were performed using an AXIS Supra spectrometer (Kratos Analytical Inc., UK), equipped with a hemispherical analyser, and a monochromatic Al K-alpha source (1487 eV) operated at 15 mA and 15 kV. The XPS spectra were acquired from an 700 x 300 μm^2 area, with a take-off angle of 90°. Pass energies of 160 eV and 20 eV were used for survey and high-resolution scans, respectively. The sample was depth-profiled using an Ar Gas Cluster Ion Source (GCIS, Kratos Analytical Inc., Minibeam 6) operated at 10 keV, Ar_{1000}^+, with a raster size of 2 x 2 mm^2. The XPS spectra were acquired after progressive etch cycles of 30 s. The sample was electrically grounded to the sample holder to prevent charge build-up on the sample surface. To determine the work functions and energy levels of the sample, UPS measurements were carried out using the same instrument, with a He(I) source (hv = 21.22 eV), an analysis area of 55 µm, and a pass energy of 10 eV. The UPS analysis was performed on the sample that has been electrically grounded, with additional –9 V bias applied to the sample.

X-ray crystallography. Single crystals were mounted on a Bruker X8 Quest CPAD area detector diffractometer and data was collected at 100 K using an IµS 3.0 Microfocus Mo-Kα radiation source (λ = 0.71073 Å). Data reduction and absorption corrections were performed using the SAINT and SADABS software packages, respectively. All structures were solved by direct methods and refined by full-matrix least squares procedures on F^2, using the Bruker SHELXTL-2014 software package.[78] Non-hydrogen atoms were anisotropically refined, after which hydrogen atoms were introduced at calculated positions and subsequent further refinement of the data performed. Graphical depictions of the crystal structures were created using the programs Mercury and VESTA.[79] Off-center displacement of the metal center in each 2D perovskite was determined by defining a centroid of the $[MX_6]^{2-}$ octahedra, followed by measuring the distance of the metal ions from the defined centroid.

Analysis of structural distortions in 2D perovskites. Distortion of the octahedral $[SnI_6]^{4-}$ inorganic building blocks of the materials were evaluated using the following parameters:

Bond length distortion:[80]

$$\Delta_{oct} = \frac{1}{6}\sum_{i=1}^{6}\left[\frac{d_i - d_m}{d_m}\right]^2 \quad (1)$$

Octahedral elongation:[81-82]

$$\lambda_{oct} = \frac{1}{6}\sum_{i=1}^{6}\left[\frac{d_i}{d_0}\right]^2 \quad (2)$$

Octahedral angle variance: [80-83]

$$\sigma^2_{oct} = \frac{1}{11}\sum_{i=1}^{12}(\alpha_i - 90)^2 \quad (3)$$

where d_i = Individual Sn–I bond length, d_m = average Sn–I bond length, d_o = center-to-vertex distance of a regular polyhedron of the same volume, and α_i = individual I–Sn–I angles. The parameters Δ_{oct}, λ_{oct} and σ^2_{oct} provide a quantitative measure of polyhedral distortion, independent of the effective size of the polyhedron. The software VESTA was used in calculation of λ_{oct} and σ^2_{oct}.

Glancing angle X-ray diffraction. Glancing-angle X-ray diffraction measurements were conducted using a Bruker AXS D8 ADVANCE system with Cu-Kα radiation (λ = 1.5418 Å). The XRD spectra were recorded with an incident angle of 5 °, a step size of 0.05 °, and a delay time of 1 s for each step.

Temperature- and power-dependent photoluminescence spectroscopies. A WITec alpha 300RAS confocal Raman microscope was used to record the photoluminescence (PL) spectra of the materials. The red line of a linearly polarized CW solid laser (wavelength = 573 nm) was used throughout. In order to avoid photodegradation of the sample and saturation of the detector, steady-state and temperature-dependent PL measurements were conducted with an excitation power < 0.8 μW. A long working distance, 20× microscope objective (spot size of ~2 μm) was used for the low temperature experiments. Temperature-dependent measurements were conducted in the range 80 – 293 K, using a nitrogen gas flow cryostat. Power-dependent measurements were conducted by varying laser power between 0.017 and 5 μW. To avoid degradation of the materials by oxygen, the sample chamber was continuously purged with nitrogen gas throughout the measurements.

Solar cell devices and incident photon-to-current efficiencies. Photovoltaic characteristics of the solar cell devices were measured in the reverse scanning direction (from V_{oc} to J_{sc}), with a sweep rate of 100 mV s^{-1}, under AM1.5G (100 mW cm^{-2}) spectral irradiation from a solar simulator (Newport 91190A) incorporating a 450 W xenon lamp (model 81172, Oriel) calibrated with a Si reference cell (Oriel PN91150). Devices were characterized through a 0.08 cm^2 black mask. Incident photon-to-current efficiency (IPCE) was measured using a PVE300 (Bentham) photovoltaic quantum efficiency (QE) instrument, possessing a dual xenon/quartz halogen light source, in DC mode, and with no bias light in the wavelength range 300 – 800 nm. A Coherent OPerA Solo optical parametric amplifier pumped with a Coherent Libra™ regenerative amplifier (50 fs, 1 kHz, 800 nm) was used to generate a 600 nm excitation beam.

Poling measurements. Interdigitated FTO electrodes (3 Fingers) with lateral spacing of 100 μm and total effective length of 3.17 cm was used in fabrication of lateral device, as shown in **Figure S14**. Perovskite active material (300 nm thick) was spin coated as described in the thin film formation section. The measurements were conducted in a probe station chamber under vacuum of 10^{-6} mbar with the light incident through a quartz window. A monochromatic blue LED of wavelength 445 nm and power 1400 W m^{-2} was used for the photocurrent measurements. Electrical properties were measured using a Keithley 4200-SCS semiconductor characterization system. The electric field applied on the perovskite film is 2 V μm^{-1} in the dark. After poling, the current-voltage (*I-V*) and current-time (*I-t*) curves were measured using the Keithley 4200-SCS.

Density functional theory (DFT) calculations. To explore the electronic and optical properties of ImEA[PbI_4] and ImEA[SnI_4], electronic structure calculations were systematically performed within the framework of the DFT formalism,[84-85] using the projector augmented wave (PAW)[86] method implemented in the Vienna *ab Initio* Simulation Package (VASP).[87] The structures of ImEA[PbI_4] and ImEA[SnI_4] contain 40 C, 88 H, 24 N, 8 Pb, 32 I atoms and 40 C, 88 H, 24 N, 8 Sn, 32 I atoms, respectively. The PAW pseudopotentials for C, H, N, Pb, Sn, and I have valence states $2s^22p^2$, $1s^1$, $2s^22p^3$, $6s^26p^2$, $5s^25p^2$, and $5s^25p^5$, respectively. The energy cut-off used throughout the calculations is set at 500 eV, while the Brillouin zone has been sampled using a 3 × 3 × 3 Monkhorst-Pack k-point grid[88] for ionic relaxation of the system. We have used the generalized gradient approximations (GGA) exchange correlation functional of Perdew-Burke-Ernzerhof (PBE).[89] The Density of States (DOS) and optical absorption for both the systems have been determined for the minimum energy configuration. For the optical absorption spectra calculations, the number of bands is taken double accounting for both occupied and unoccupied states.

ASSOCIATED CONTENT

Supporting Information

The Supporting Information is available free of charge on the ACS Publications website. Crystal structures of hybrid lead iodide perovskites (cif files). Additional crystallographic and structure refinement data, plus selected bond lengths and bond angles, DFT-calculated UV-vis absorption spectra and density of states, temperature-dependent PL spectra, Tauc plot, SEM, AFM, GAXRD, XPS, additional device data, and poling measurements (pdf).

A preprint version of this manuscript (prior to peer-review) can be found in the ChemRxiv Preprint Server.[90]

The authors declare no competing financial interest.

AUTHOR INFORMATION

Corresponding Author

* E-mail: jengland@ntu.edu.sg.
* E-mail: nripan@ntu.edu.sg.

* E-mail: zexiang@ntu.edu.sg.
* E-mail: sudip@iiti.ac.in, sudiphys@gmail.com.

Notes

CIF data for associated crystal structures have been deposited in the Cambridge Crystallographic Data Centre under deposition numbers CCDC 1949805 – 1949812.

ACKNOWLEDGMENT

We would like to thank Prof. Subodh G. Mhaisalkar for providing access to the facilities of the Energy Research Institute @ NTU (ERI@N). JE is grateful to NTU for funding (M4081442). SGM, NM, BF, TMK, and TJNH would like to acknowledge funding from the Singapore National Research Foundation through the Intra-CREATE Collaborative Program (NRF2018-ITC001-001), Office of Naval Research Global (ONRG-NICOP-N62909-17-1-2155), and the Competitive Research Program: NRF–CRP14–2014–03. YL and ZXS would like to acknowledge Ministry of Education of Singapore for the funding through AcRF Tier 1 (ref. RG195/ 17 and RG 156/19). JK and SC acknowledge the fellowship from IIT Indore and computing time from NSCC, Singapore. TJNH would like to acknowledge the Center of High Field NMR Spectroscopy and Imaging (NTU) for the use of their facilities.

REFERENCES

1. Best Research-Cell Efficiencies. https://www.nrel.gov/pv/assets/pdfs/best-research-cell-efficiencies.20200803.pdf (accessed August 31st, 2020).
2. Jiang, Y.; Qiu, L.; Juarez-Perez, E. J.; Ono, L. K.; Hu, Z.; Liu, Z.; Wu, Z.; Meng, L.; Wang, Q.; Qi, Y. Reduction of Lead Leakage from Damaged Lead Halide Perovskite Solar Modules Using Self-Healing Polymer-Based Encapsulation. *Nat. Energy* **2019**, *4 (7)*, 585-593.
3. Chen, M.; Ju, M. G.; Garces, H. F.; Carl, A. D.; Ono, L. K.; Hawash, Z.; Zhang, Y.; Shen, T.; Qi, Y.; Grimm, R. L.; Pacifici, D.; Zeng, X. C.; Zhou, Y.; Padture, N. P., Highly Stable and Efficient All-Inorganic Lead-Free Perovskite Solar Cells with Native-Oxide Passivation. *Nat Commun* **2019,** *10* (1), 16.
4. Nakamura, T.; Yakumaru, S.; Truong, M. A.; Kim, K.; Liu, J.; Hu, S.; Otsuka, K.; Hashimoto, R.; Murdey, R.; Sasamori, T.; Kim, H. D.; Ohkita, H.; Handa, T.; Kanemitsu, Y.; Wakamiya, A. Sn(IV)-Free Tin Perovskite Films Realized by *in Situ* Sn(0) Nanoparticle Treatment of the Precursor Solution. *Nat. Commun.* **2020**, *11 (1)*, 3008.
5. Liu, X.; Wang, Y.; Wu, T.; He, X.; Meng, X.; Barbaud, J.; Chen, H.; Segawa, H.; Yang, X.; Han, L. Efficient and Stable Tin Perovskite Solar Cells Enabled by Amorphous-Polycrystalline Structure. *Nat. Commun.* **2020**, *11 (1)*, 2678.
6. Jiang, X.; Wang, F.; Wei, Q.; Li, H.; Shang, Y.; Zhou, W.; Wang, C.; Cheng, P.; Chen, Q.; Chen, L.; Ning, Z. Ultra-High Open-Circuit Voltage of Tin Perovskite Solar Cells *via* an Electron Transporting Layer Design. *Nat. Commun.* **2020**, *11 (1)*, 1245.
7. Stoumpos, C. C.; Frazer, L.; Clark, D. J.; Kim, Y. S.; Rhim, S. H.; Freeman, A. J.; Ketterson, J. B.; Jang, J. I.; Kanatzidis, M. G. Hybrid Germanium Iodide Perovskite Semiconductors: Active Lone Pairs, Structural Distortions, Direct and Indirect Energy Gaps, and Strong Nonlinear Optical Properties. *J. Am. Chem. Soc.* **2015**, *137 (21)*, 6804-6819.
8. Stoumpos, C. C.; Mao, L.; Malliakas, C. D.; Kanatzidis, M. G. Structure-Band Gap Relationships in Hexagonal Polytypes and Low-Dimensional Structures of Hybrid Tin Iodide Perovskites. *Inorg. Chem.* **2017**, *56 (1)*, 56-73.
9. Ke, W.; Stoumpos, C. C.; Kanatzidis, M. G. "Unleaded" Perovskites: Status Quo and Future Prospects of Tin-Based Perovskite Solar Cells. *Adv. Mater.* **2019**, *31*, 1803230.
10. Kumar, M. H.; Dharani, S.; Leong, W. L.; Boix, P. P.; Prabhakar, R. R.; Baikie, T.; Shi, C.; Ding, H.; Ramesh, R.; Asta, M.; Graetzel, M.; Mhaisalkar, S. G.; Mathews, N. Lead-Free Halide Perovskite Solar Cells with High Photocurrents Realized through Vacancy Modulation. *Adv. Mater.* **2014**, *26 (41)*, 7122-7127.
11. Tai, Q.; Guo, X.; Tang, G.; You, P.; Ng, T. W.; Shen, D.; Cao, J.; Liu, C. K.; Wang, N.; Zhu, Y.; Lee, C. S.; Yan, F. Antioxidant Grain Passivation for Air-Stable Tin-Based Perovskite Solar Cells. *Angew. Chem. Int. Ed.* **2019**, *58 (3)*, 806-810.
12. Song, T. B.; Yokoyama, T.; Stoumpos, C. C.; Logsdon, J.; Cao, D. H.; Wasielewski, M. R.; Aramaki, S.; Kanatzidis, M. G. Importance of Reducing Vapor Atmosphere in the Fabrication of Tin-Based Perovskite Solar Cells. *J. Am. Chem. Soc.* **2017**, *139 (2)*, 836-842.
13. Gu, F.; Ye, S.; Zhao, Z.; Rao, H.; Liu, Z.; Bian, Z.; Huang, C. Improving Performance of Lead-Free Formamidinium Tin Triiodide Perovskite Solar Cells by Tin Source Purification. *Sol. RRL* **2018**, *2 (10)*, 1800136.
14. Gao, W.; Ran, C.; Li, J.; Dong, H.; Jiao, B.; Zhang, L.; Lan, X.; Hou, X.; Wu, Z. Robust Stability of Efficient Lead-Free Formamidinium Tin Iodide Perovskite Solar Cells Realized by Structural Regulation. *J. Phys. Chem. Lett.* **2018**, *9 (24)*, 6999-7006.
15. Prasanna, R.; Gold-Parker, A.; Leijtens, T.; Conings, B.; Babayigit, A.; Boyen, H. G.; Toney, M. F.; McGehee, M. D. Band Gap Tuning *via* Lattice Contraction and Octahedral Tilting in Perovskite Materials for Photovoltaics. *J. Am. Chem. Soc.* **2017**, *139 (32)*, 11117-11124.
16. Cheng, Z.; Lin, J. Layered Organic–Inorganic Hybrid Perovskites: Structure, Optical Properties, Film Preparation, Patterning and Templating Engineering. *CrystEngComm* **2010**, *12 (10)*, 2646-2662.
17. Saparov, B.; Mitzi, D. B. Organic-Inorganic Perovskites: Structural Versatility for Functional Materials Design. *Chem. Rev.* **2016**, *116 (7)*, 4558-4596.
18. Passarelli, J. V.; Fairfield, D. J.; Sather, N. A.; Hendricks, M. P.; Sai, H.; Stern, C. L.; Stupp, S. I. Enhanced Out-of-Plane Conductivity and Photovoltaic Performance in $n = 1$ Layered Perovskites through Organic Cation Design. *J. Am. Chem. Soc.* **2018**, *140 (23)*, 7313-7323.
19. Li, Y.; Zhao, Y.; Cheng, H.; Zhao, K.; Wang, Z. S. Highly Efficient and Stable Pure Two-Dimensional Perovskite-Based Solar Cells with the 3-Aminopropionitrile Organic Cation. *ACS Appl. Mater. Interfaces* **2020**, *12 (16)*, 18590-18595.
20. Lin, Y.; Bai, Y.; Fang, Y.; Wang, Q.; Deng, Y.; Huang, J. Suppressed Ion Migration in Low-Dimensional Perovskites. *ACS Energy Lett.* **2017**, *2 (7)*, 1571-1572.
21. Huang, Z.; Proppe, A. H.; Tan, H.; Saidaminov, M. I.; Tan, F.; Mei, A.; Tan, C.-S.; Wei, M.; Hou, Y.; Han, H.; Kelley, S. O.; Sargent, E. H. Suppressed Ion Migration in Reduced-Dimensional Perovskites Improves Operating Stability. *ACS Energy Lett.* **2019**, *4 (7)*, 1521-1527.
22. Mao, L.; Stoumpos, C. C.; Kanatzidis, M. G. Two-Dimensional Hybrid Halide Perovskites: Principles and Promises. *J. Am. Chem. Soc.* **2019**, *141 (3)*, 1171-1190.
23. Smith, M. D.; Connor, B. A.; Karunadasa, H. I. Tuning the Luminescence of Layered Halide Perovskites. *Chem. Rev.* **2019**, *119 (5)*, 3104-3139.

24. Cao, D. H.; Stoumpos, C. C.; Farha, O. K.; Hupp, J. T.; Kanatzidis, M. G. 2D Homologous Perovskites as Light-Absorbing Materials for Solar Cell Applications. *J. Am. Chem. Soc.* **2015**, *137 (24)*, 7843-7850.
25. Koh, T. M.; Shanmugam, V.; Schlipf, J.; Oesinghaus, L.; Muller-Buschbaum, P.; Ramakrishnan, N.; Swamy, V.; Mathews, N.; Boix, P. P.; Mhaisalkar, S. G. Nanostructuring Mixed-Dimensional Perovskites: A Route toward Tunable, Efficient Photovoltaics. *Adv. Mater.* **2016**, *28 (19)*, 3653-3661.
26. Febriansyah, B.; Koh, T. M.; Lekina, Y.; Jamaludin, N. F.; Bruno, A.; Ganguly, R.; Shen, Z. X.; Mhaisalkar, S. G.; England, J. Improved Photovoltaic Efficiency and Amplified Photocurrent Generation in Mesoporous *n* = 1 Two-Dimensional Lead–Iodide Perovskite Solar Cells. *Chem. Mater.* **2019**, *31 (3)*, 890-898.
27. Zimmermann, I.; Aghazada, S.; Nazeeruddin, M. K. Lead and HTM Free Stable Two-Dimensional Tin Perovskites with Suitable Band Gap for Solar Cell Applications. *Angew. Chem. Int. Ed.* **2019**, *58 (4)*, 1072-1076.
28. Guan, J.; Tang, Z.; Guloy, A. M. α-$[NH_3(CH_2)_5NH_3]SnI_4$: A New Layered Perovskite Structure. *Chem. Commun.* **1999**, *18*, 1833–1834.
29. Mao, L.; Tsai, H.; Nie, W.; Ma, L.; Im, J.; Stoumpos, C. C.; Malliakas, C. D.; Hao, F.; Wasielewski, M. R.; Mohite, A. D.; Kanatzidis, M. G. Role of Organic Counterion in Lead- and Tin-Based Two-Dimensional Semiconducting Iodide Perovskites and Application in Planar Solar Cells. *Chem. Mater.* **2016**, *28 (21)*, 7781-7792.
30. Febriansyah, B.; Giovanni, D.; Ramesh, S.; Koh, T. M.; Li, Y.; Sum, T. C.; Mathews, N.; England, J. Inducing Formation of a Corrugated, White-Light Emitting 2D Lead-Bromide Perovskite *via* Subtle Changes in Templating Cation. *J. Mater. Chem. C* **2020**, *8 (3)*, 889-893.
31. Xu, Z.; Mitzi, D. B.; Medeiros, D. R. $[(CH_3)_3NCH_2CH_2NH_3]SnI_4$: A Layered Perovskite with Quaternary/Primary Ammonium Dications and Short Interlayer Iodine–Iodine Contacts. *Inorg. Chem.* **2003**, *42 (5)*, 1400-1402.
32. Takahashi, Y.; Obara, R.; Nakagawa, K.; Nakano, M.; Tokita, J.; Inabe, T. Tunable Charge Transport in Soluble Organic–Inorganic Hybrid Semiconductors. *Chem. Mater.* **2007**, *19 (25)*, 6312–6316.
33. Tang, Z.; Guan, J.; Guloy, A. M. Synthesis and Crystal Structure of New Organic-Based Layered Perovskites with 2,2′-Biimidazolium Cations. *J. Mater. Chem.* **2001**, *11 (2)*, 479-482.
34. Zimmermann, I.; Keene, T. D.; Hauser, J.; Decurtins, S.; Liu, S. X. Crystal Structures of Isotypic Poly[bis-(benz-imid-azolium) [tetra-μ-iodido-stannate(II)]] and Poly[bis-(5,6-di-fluoro-benzimidazolium) [tetra-μ-iodido-stannate(II)]]. *Acta Crystallogr. Sect. E Struct. Rep. Online* **2014**, *70 (Pt 10)*, 178-182.
35. Febriansyah, B.; Lekina, Y.; Ghosh, B.; Harikesh, P. C.; Koh, T. M.; Li, Y.; Shen, Z.; Mathews, N.; England, J. Molecular Engineering of Pure 2D Lead-Iodide Perovskite Solar Absorbers Displaying Reduced Band Gaps and Dielectric Confinement. *ChemSusChem* **2020**, *13 (10)*, 2693-2701.
36. Febriansyah, B.; Borzda, T.; Cortecchia, D.; Neutzner, S.; Folpini, G.; Koh, T. M.; Li, Y.; Mathews, N.; Petrozza, A.; England, J. Metal Coordination Sphere Deformation Induced Highly Stokes-Shifted, Ultra Broadband Emission in 2D Hybrid Lead-Bromide Perovskites and Investigation of Its Origin. *Angew. Chem. Int. Ed.* **2020**, *59 (27)*, 10791-10796.
37. Seshadri, R. Visualizing Lone Pairs in Compounds Containing Heavier Congeners of the Carbon and Nitrogen Group Elements. *Proc. Indian Acad. Sci. (Chem. Sci.)* **2001**, *113 (5 & 6)*, 487-496.
38. Bersuker, I. B. Pseudo-Jahn-Teller Effect -A Two-State Paradigm in Formation, Deformation, and Transformation of Molecular Systems and Solids. *Chem. Rev.* **2013**, *113 (3)*, 1351-1390.
39. Walsh, A.; Payne, D. J.; Egdell, R. G.; Watson, G. W. Stereochemistry of Post-Transition Metal Oxides: Revision of the Classical Lone Pair Model. *Chem. Soc. Rev.* **2011**, *40 (9)*, 4455-4463.
40. Watson, G. W.; Parker, S. C.; Kresse, G. *Ab Initio* Calculation of the Origin of the Distortion of α-PbO. *Phys. Rev. B* **1999**, *59 (13)*, 8481-8486.
41. Waghmare, U. V.; Spaldin, N. A.; Kandpal, H. C.; Seshadri, R. First-Principles Indicators of Metallicity and Cation Off-Centricity in the IV-VI Rocksalt Chalcogenides of Divalent Ge, Sn, and Pb. *Phys. Rev. B* **2003**, *67 (12)*, 125111.
42. Brown, I. D. Bond Valence as an Aid to Understanding the Stereochemistry of O and F Complexes of Sn(II), Sb(III), Te(IV), I(V) and Xe(VI). *J. Solid State Chem.* **1974**, *11 (3)*, 214-233.
43. Fabini, D. H.; Seshadri, R.; Kanatzidis, M. G. The Underappreciated Lone Pair in Halide Perovskites Underpins Their Unusual Properties. *MRS Bull.* **2020**, *45 (6)*, 467-477.
44. Wang, S.; Mitzi, D. B.; Feild, C. A.; Guloy, A. Synthesis and Characterization of $[NH_2C(I){:}NH_2]_3MI_5$ (M = Sn, Pb): Stereochemical Activity in Divalent Tin and Lead Halides Containing Single <110> Perovskite Sheets. *J. Am. Chem. Soc.* **1995**, *117 (19)*, 5297-5302
45. Laurita, G.; Fabini, D. H.; Stoumpos, C. C.; Kanatzidis, M. G.; Seshadri, R., Chemical Tuning of Dynamic Cation Off-Centering in the Cubic Phases of Hybrid Tin and Lead Halide Perovskites. *Chem. Sci.* **2017**, *8 (8)*, 5628-5635.
46. Wheeler, R. A.; Kumar, P. N. V. P. Stereochemically Active or Inactive Lone Pair Electrons in Some Six-Coordinate, Group 15 Halides. *J. Am. Chem. Soc.* **1992**, *114 (12)*, 4776-4784.
47. Atanasov, M.; Reinen, D. Predictive Concept for Lone-Pair Distortions - DFT and Vibronic Model Studies of $AX_n^{-(n-3)}$ Molecules and Complexes ($A = N^{III}$ to Bi^{III}; $X = F^{-I}$ to I^{-I}; n = 3-6). *J. Am. Chem. Soc.* **2002**, *124 (23)*, 6693-6705.
48. Walsh, A.; Watson, G. W. Influence of the Anion on Lone Pair Formation in Sn(II) Monochalcogenides: A DFT Study. *J. Phys. Chem. B* **2005**, *109 (40)*, 18868-18875.
49. Phuyal, D.; Safdari, M.; Pazoki, M.; Liu, P.; Philippe, B.; Kvashnina, K. O.; Karis, O.; Butorin, S. M.; Rensmo, H.; Edvinsson, T.; Kloo, L.; Gardner, J. M. Electronic Structure of Two-Dimensional Lead(II) Iodide Perovskites: An Experimental and Theoretical Study. *Chem. Mater.* **2018**, *30 (15)*, 4959-4967.
50. Knutson, J. L.; Martin, J. D.; Mitzi, D. B. Tuning the Band Gap in Hybrid Tin Iodide Perovskite Semiconductors Using Structural Templating. *Inorg. Chem.* **2005**, *44 (13)*, 4699-4705.
51. Dohner, E. R.; Hoke, E. T.; Karunadasa, H. I. Self-Assembly of Broadband White-Light Emitters. *J. Am. Chem. Soc.* **2014**, *136 (5)*, 1718-1721.
52. Mao, L.; Wu, Y.; Stoumpos, C. C.; Wasielewski, M. R.; Kanatzidis, M. G. White-Light Emission and Structural Distortion in New Corrugated Two-Dimensional Lead Bromide Perovskites. *J. Am. Chem. Soc.* **2017**, *139 (14)*, 5210-5215.
53. Chen, Q.; De Marco, N.; Yang, Y.; Song, T.-B.; Chen, C.-C.; Zhao, H.; Hong, Z.; Zhou, H.; Yang, Y. Under the Spotlight: The Organic–Inorganic Hybrid Halide Perovskite for Optoelectronic Applications. *Nano Today* **2015**, 10 (3), 355-396.

54. Tao, S.; Schmidt, I.; Brocks, G.; Jiang, J.; Tranca, I.; Meerholz, K.; Olthof, S. Absolute Energy Level Positions in Tin- and Lead-Based Halide Perovskites. *Nat. Commun.* 2019, 10 (1), 2560.
55. Pazoki, M.; Edvinsson, T. Metal Replacement in Perovskite Solar Cell Materials: Chemical Bonding Effects and Optoelectronic Properties. *Sustain. Energy & Fuels* **2018**, *2 (7)*, 1430-1445.
56. Mitzi, D. B. Synthesis, Crystal Structure, and Optical and Thermal Properties of $(C_4H_9NH_3)_2MI_4$ (M = Ge, Sn, Pb). *Chem. Mater.* **1996**, *8 (3)*, 791-800.
57. Lanzetta, L.; Marin-Beloqui, J. M.; Sanchez-Molina, I.; Ding, D.; Haque, S. A. Two-Dimensional Organic Tin Halide Perovskites with Tunable Visible Emission and Their Use in Light-Emitting Devices. *ACS Energy Lett.* **2017**, *2 (7)*, 1662-1668.
58. Smith, M. D.; Karunadasa, H. I. White-Light Emission from Layered Halide Perovskites. *Acc. Chem. Res.* **2018**, *51 (3)*, 619-627.
59. Papavassiliou, G. C.; Koutselas, I. B.; Terzis, A.; Whangbo, M.-H. Structural and Electronic Properties of the Natural Quantum-Well System $(C_6H_5CH_2CH_2NH_3)_2SnI_4$. *Solid State Commun.* **1994**, *91 (9)*, 695-698.
60. Hong, X.; Ishihara, T.; Nurmikko, A. V., Dielectric Confinement Effect on Excitons in PbI_4-Based Layered Semiconductors. *Phys. Rev. B* **1992**, *45 (12)*, 6961-6964.
61. Huang, L.-y.; Lambrecht, W. R. L. Electronic Band Structure, Phonons, and Exciton Binding Energies of Halide Perovskites $CsSnCl_3$, $CsSnBr_3$, and $CsSnI_3$. *Phys. Rev. B* **2013**, *88 (16)*, 165203.
62. Tanaka, K.; Kondo, T. Bandgap and Exciton Binding Energies in Lead-Iodide-Based Natural Quantum-Well Crystals. *Sci. Tech. Adv. Mater.* **2004**, *4 (6)*, 599-604.
63. Maughan, A. E.; Kurzman, J. A.; Neilson, J. R. Hybrid Inorganic-Organic Materials with an Optoelectronically Active Aromatic Cation: $(C_7H_7)_2SnI_6$ and $C_7H_7PbI_3$. *Inorg. Chem.* **2015**, *54 (1)*, 370-8.
64. Febriansyah, B.; Koh, T. M.; John, R. A.; Ganguly, R.; Li, Y.; Bruno, A.; Mhaisalkar, S. G.; England, J. Inducing Panchromatic Absorption and Photoconductivity in Polycrystalline Molecular 1D Lead-Iodide Perovskites through π-Stacked Viologens. *Chem. Mater.* **2018**, *30 (17)*, 5827-5830.
65. Wang, R.; Wang, J.; Tan, S.; Duan, Y.; Wang, Z.-K.; Yang, Y., Opportunities and Challenges of Lead-Free Perovskite Optoelectronic Devices. *Trends in Chemistry* **2019**, *1 (4)*, 368-379.
66. Jung, M.-C.; Raga, S. R.; Qi, Y. Properties and Solar Cell Applications of Pb-Free Perovskite Films Formed by Vapor Deposition. *RSC Adv.* **2016**, *6 (4)*, 2819-2825.
67. Chen, C.-C.; Bae, S.-H.; Chang, W.-H.; Hong, Z.; Li, G.; Chen, Q.; Zhou, H.; Yang, Y. Perovskite/Polymer Monolithic Hybrid Tandem Solar Cells Utilizing a Low-Temperature, Full Solution Process. *Mater. Horiz.* **2015**, *2 (2)*, 203-211.
68. Yu, J. C.; Hong, J. A.; Jung, E. D.; Kim, D. B.; Baek, S. M.; Lee, S.; Cho, S.; Park, S. S.; Choi, K. J.; Song, M. H. Highly Efficient and Stable Inverted Perovskite Solar Cell Employing PEDOT:GO Composite Layer as a Hole Transport Layer. *Sci. Rep.* **2018**, *8 (1)*, 1070.
69. Dong, H.; Wu, Z.; Xia, B.; Xi, J.; Yuan, F.; Ning, S.; Xiao, L.; Hou, X., Modified Deposition Process of Electron Transport Layer for Efficient Inverted Planar Perovskite Solar Cells. *Chem. Commun.* **2015**, *51 (43)*, 8986-9.
70. Xiao, X.; Dai, J.; Fang, Y.; Zhao, J.; Zheng, X.; Tang, S.; Rudd, P. N.; Zeng, X. C.; Huang, J. Suppressed Ion Migration along the In-Plane Direction in Layered Perovskites. *ACS Energy Lett.* **2018**, *3 (3)*, 684-688.
71. Xiao, Z.; Yuan, Y.; Shao, Y.; Wang, Q.; Dong, Q.; Bi, C.; Sharma, P.; Gruverman, A.; Huang, J. Giant Switchable Photovoltaic Effect in Organometal Trihalide Perovskite Devices. *Nat. Mater.* **2014**, *14 (2)*, 193-198.
72. Zhang, F.; Kim, D. H.; Lu, H.; Park, J. S.; Larson, B. W.; Hu, J.; Gao, L.; Xiao, C.; Reid, O. G.; Chen, X.; Zhao, Q.; Ndione, P. F.; Berry, J. J.; You, W.; Walsh, A.; Beard, M. C.; Zhu, K. Enhanced Charge Transport in 2D Perovskites *via* Fluorination of Organic Cation. *J. Am. Chem. Soc.* **2019**, *141 (14)*, 5972-5979.
73. Safdari, M.; Svensson, P. H.; Hoang, M. T.; Oh, I.; Kloo, L.; Gardner, J. M. Layered 2D Alkyldiammonium Lead Iodide Perovskites: Synthesis, Characterization, and Use in Solar Cells. *J. Mater. Chem. A* **2016**, *4 (40)*, 15638-15646.
74. Lin, R.; Xiao, K.; Qin, Z.; Han, Q.; Zhang, C.; Wei, M.; Saidaminov, M. I.; Gao, Y.; Xu, J.; Xiao, M.; Li, A.; Zhu, J.; Sargent, E. H.; Tan, H., Monolithic All-Perovskite Tandem Solar Cells with 24.8% Efficiency Exploiting Comproportionation to Suppress Sn(ii) Oxidation in Precursor Ink. *Nat. Energy* **2019,** *4* (10), 864-873.
75. Xiao, K.; Lin, R.; Han, Q.; Hou, Y.; Qin, Z.; Nguyen, H. T.; Wen, J.; Wei, M.; Yeddu, V.; Saidaminov, M. I.; Gao, Y.; Luo, X.; Wang, Y.; Gao, H.; Zhang, C.; Xu, J.; Zhu, J.; Sargent, E. H.; Tan, H., All-Perovskite Tandem Solar Cells with 24.2% Certified Efficiency and Area Over 1 cm^2 using Surface-Anchoring Zwitterionic Antioxidant. *Nature Energy* **2020,** *5* (11), 870-880.
76. Massiot, D.; Fayon, F.; Capron, M.; King, I.; Le Calvé, S.; Alonso, B.; Durand, J.-O.; Bujoli, B.; Gan, Z.; Hoatson, G., Modelling One- and Two-Dimensional Solid-State NMR Spectra. *Mag. Res. Chem.* **2002,** *40* (1), 70-76.
77. Hooper, T. J. N.; Partridge, T. A.; Rees, G. J.; Keeble, D. S.; Powell, N. A.; Smith, M. E.; Mikheenko, I. P.; Macaskie, L. E.; Bishop, P. T.; Hanna, J. V., Direct Solid State NMR Observation of the $^{(105)}$Pd Nucleus in Inorganic Compounds and Palladium Metal Systems. *Phys. Chem. Chem. Phys.* **2018,** *20* (41), 26734-26743.
78. Sheldrick, G. M., A Short History of SHELX. *Acta Crystallogr. A* **2008,** *64* (Pt 1), 112-122.
79. Momma, K.; Izumi, F. An Integrated Three-Dimensional Visualization System VESTA Using wxWidgets. *Commission on Crystallogr. Comput.* **2006**, *7*, 106–119.
80. Ertl, A.; Hughes, J. M.; Pertlik, F.; Jr., F. F. F.; Wright, S. E.; Brandstatter, F.; Marler, B. Polyhedron Distortions in Tourmaline. *Can. Mineral.,* **2002**, *40*, 153–162.
81. Robinson, K.; Gibbs, G. V.; Ribbe, P. H. Quadratic Elongation: A Quantitative Measure of Distortion in Coordination Polyhedra. *Science* **1971**, *172*, 567–570.
82. Thomas, N. W. Crystal Structure-Physical Property Relationships in Perovskites. *Acta Crystallogr. B* **1989**, *45*, 337–344.
83. Fleet, M. E. Distortion Parameters for Coordination Polyhedra. *Mineral. Mag.* **1976**, *40*, 531–533.
84. Hohenberg, P.; Kohn, W., Inhomogeneous Electron Gas. *Phys. Rev.* **1964,** *136* (3B), B864-B871.
85. Kohn, W.; Sham, L. J., Self-Consistent Equations including Exchange and Correlation Effects. *Phys. Rev.* **1965,** *140* (4A), A1133-A1138.
86. Kresse, G.; Furthmüller, J. Efficient Iterative Schemes for *ab Initio* Total-Energy Calculations Using a Plane-Wave Basis Set. *Phys. Rev. B*, **1996**, *54*, 11169–11186.
87. Blöchl, P. E., Projector Augmented-Wave Method. *Phys. Rev. B* **1994,** *50* (24), 17953-17979.
88. Monkhorst, H. J.; Pack, J. D., Special Points for Brillouin-Zone Integrations. *Phys. Rev. B* **1976,** *13* (12), 5188-5192.

89. Perdew, J. P.; Burke, K.; Ernzerhof, M. Generalized Gradient Approximation Made Simple. *Phys. Rev. Lett.*, **1996**, *77*, 3865–3868.
90. Febriansyah, B.; Lekina, Y.; Kaur, J.; Hooper, T. J. N.; Harikesh, P. C.; Lim, M. H.; Koh, T. M.; Chakraborty, S.; Shen, Z. X.; Mathews, N.; England, J. Formation of Corrugated 2D Tin Iodide Perovskites and Their Use as Lead-Free Solar Absorbers. 2020, ChemRxiv. Preprint. https://doi.org/10.26434/chemrxiv.12905873.v1 (accessed Sep 02, 2020).

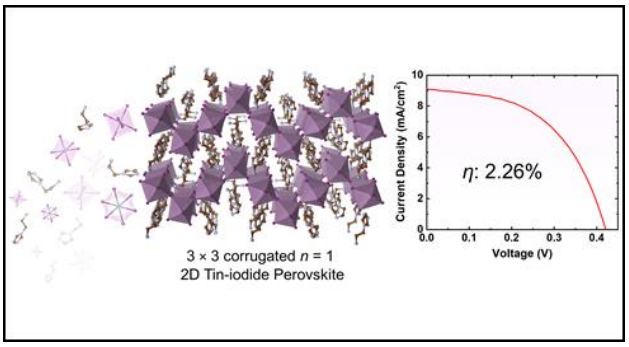
3 × 3 corrugated n = 1
2D Tin-iodide Perovskite
Current Density (mA/cm²)
Voltage (V)
η: 2.26%
0
2
4
6
8
10
0.0
0.1
0.2
0.3
0.4